Very early identification of a bimodal frictional behavior during the post-seismic phase of the 2015 M_w8.3 Illapel, Chile, earthquake

Cedric Twardzik[1,2], Mathilde Vergnolle[1], Anthony Sladen[1], and Louisa L. H. Tsang[1,3]

[1]Université Côte d'Azur, CNRS, Observatoire de la Côte d'Azur, IRD, Geoazur, UMR7329, Valbonne, France
[2]now at: Institut de Physique du Globe de Strasbourg, UMR7516, Université de Strasbourg, EOST, CNRS, Strasbourg, France
[3]now at: University of Surrey, International Study Centre, Guildford, United Kingdom

Correspondence: Cedric Twardzik (twardzik@unistra.fr)

Contents

S1 Estimated static offsets for the two largest aftershocks

Table 1. Static offsets inferred from the 30-seconds position time series for the M_w7.1 aftershock. See Figure 1 in the main text for the location of each station. We also show the theoretical duration over which the offset is smoothed because of the Kalman filter.

Station name	North (mm)	East (mm)	T_{kalman} (s)
LSCH	0.06 ± 3.09	0.09 ± 2.98	30.0
JUNT	0.01 ± 3.22	-0.35 ± 3.34	30.0
CRZL	0.08 ± 2.92	-0.10 ± 2.65	30.0
RCSD	-0.32 ± 3.21	0.36 ± 2.78	30.0
CERN	3.38 ± 3.50	0.51 ± 3.43	90.0
SANT	0.33 ± 2.85	0.01 ± 2.93	30.0
PEDR	1.00 ± 3.48	-4.53 ± 2.72	120.0
PFRJ	0.34 ± 3.00	0.24 ± 2.63	30.0
LVIL	23.71 ± 3.98	-22.02 ± 3.06	510.0
TOLO	0.52 ± 3.10	-0.88 ± 2.45	30.0
CMBA	-6.95 ± 3.15	-8.67 ± 2.76	240.0
OVLL	0.63 ± 3.45	0.30 ± 3.38	60.0
SLMC	8.28 ± 3.29	-24.55 ± 3.03	450.0
CNBA	-12.79 ± 3.05	-18.23 ± 2.75	360.0
VALL	0.02 ± 3.16	0.06 ± 3.06	30.0

Table 2. Static offsets inferred from the 30-seconds position time series for the M_w6.8 aftershock. See Figure 1 in the main text for the location of each station. We also show the theoretical duration over which the offset is smoothed because of the Kalman filter.

Station name	North (mm)	East (mm)	T_{kalman} (s)
LSCH	0.02 ± 3.09	-0.09 ± 2.98	30.0
JUNT	0.03 ± 3.22	-0.04 ± 3.34	30.0
CRZL	0.16 ± 2.92	0.40 ± 2.65	30.0
RCSD	-0.06 ± 3.21	0.34 ± 2.78	30.0
CERN	-0.22 ± 3.50	-0.17 ± 3.43	30.0
SANT	0.16 ± 2.85	-0.07 ± 2.93	30.0
PEDR	0.02 ± 3.48	-0.31 ± 2.72	30.0
PFRJ	0.01 ± 3.00	0.30 ± 2.63	30.0
LVIL	-0.24 ± 3.98	-1.99 ± 3.06	90.0
TOLO	-0.04 ± 3.10	0.19 ± 2.45	30.0
CMBA	-2.03 ± 3.15	-3.17 ± 2.76	90.0
OVLL	-0.32 ± 3.45	-0.10 ± 3.38	30.0
SLMC	-0.77 ± 3.29	-1.27 ± 3.03	120.0
CNBA	-5.67 ± 3.05	-6.93 ± 2.75	150.0
VALL	0.16 ± 3.16	-0.41 ± 3.06	30.0

S2 Post-processing of the kinematic position time series

The following figures (Figure S2.1 to S2.15) show the processing steps to obtain the hourly position time series used in this study. For each station, we show on the top row the raw position time series. The red dashed line indicates the time of the mainshock and the blue dashed lines the time of the two largest aftershock (see main text). The mean and a linear trend have been removed using the 6 days prior to the mainshock origin time. The static offset of the mainshock is also removed. The root mean square (rms) of the time series is calculated using the 6 days prior to the mainshock. The second row shows the position time series after we apply a sidereal filter that is constructed as proposed by Twardzik et al. (2019). This allows the noise level to decrease by $\sim$35% on average. The third row shows the hourly position time series used to obtain the post-seismic slip distribution over the first 12 hours (orange dots). Each position is obtained by computing the average position over a 1-hour long time window that is centered on the time of interest and that spans 30 minutes on either side. Finally, we show on the bottom row the hourly position time series after the 2 largest aftershocks are removed from the raw position time series. The figures are sorted from the northern to the southern stations.

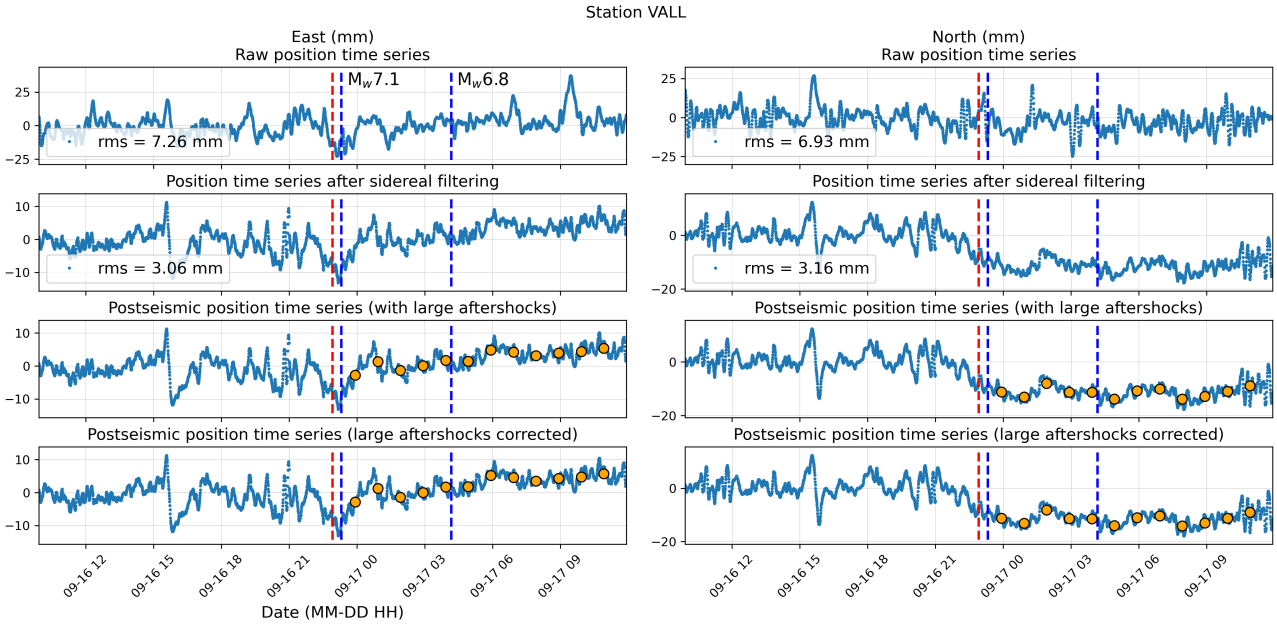

Figure S2.1. Same as Figure 2 in the main text.

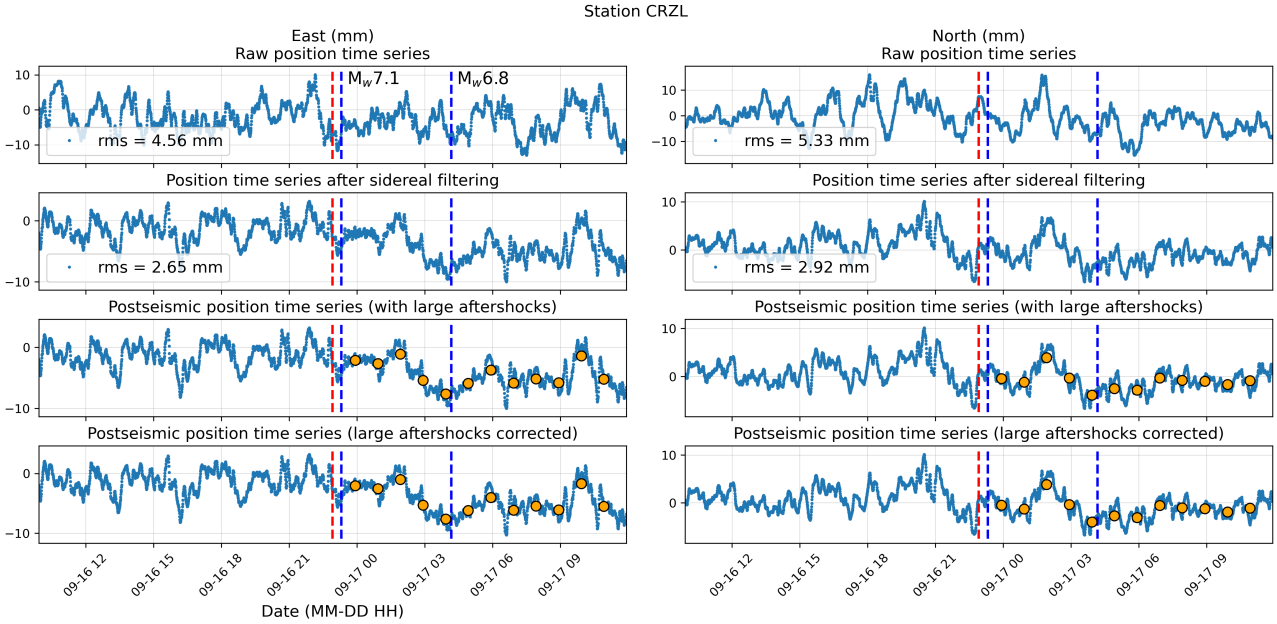

Figure S2.2. Same as Figure 2 in the main text.

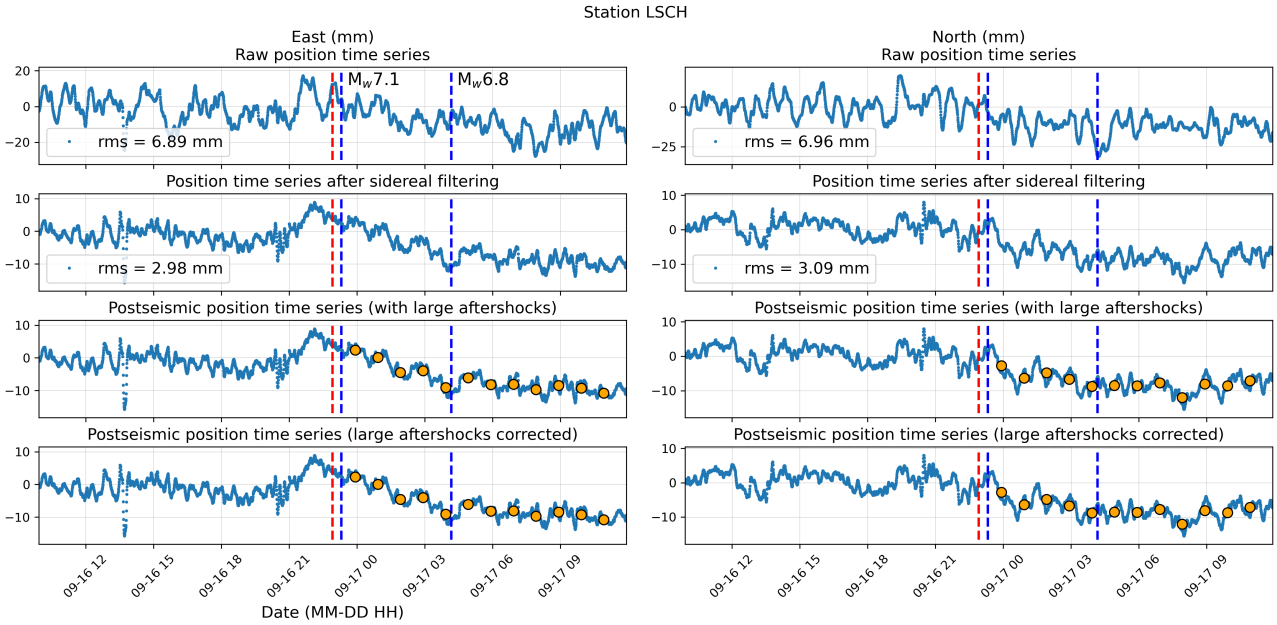

Figure S2.3. Same as Figure 2 in the main text.

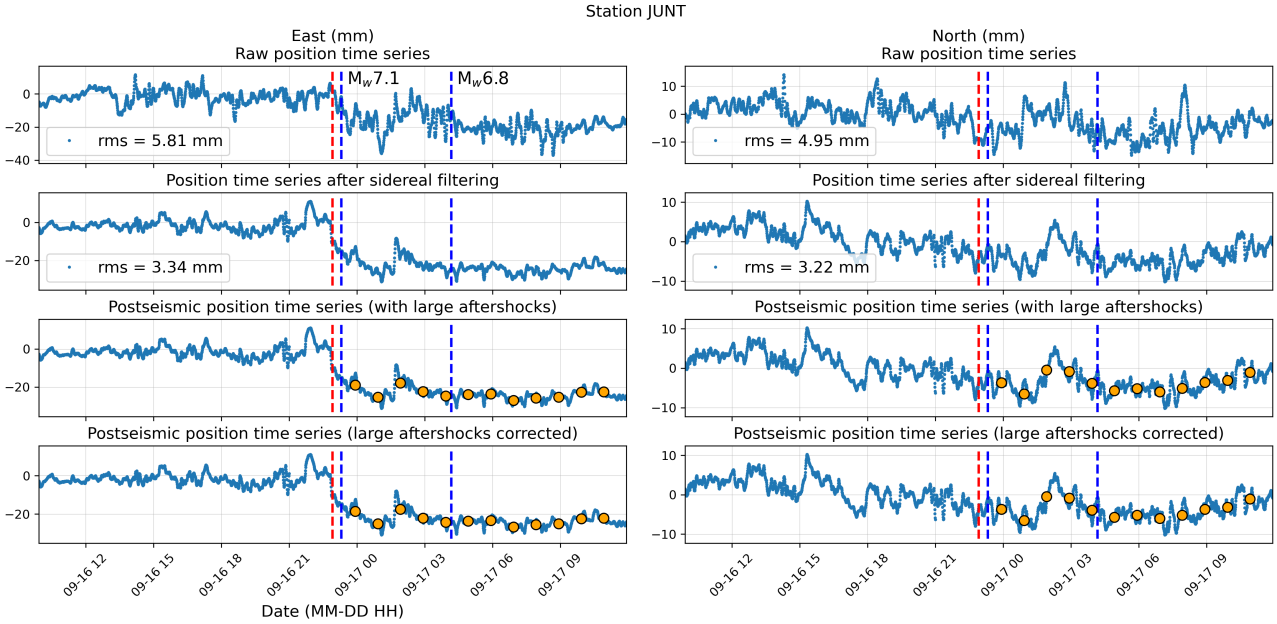

Figure S2.4. Same as Figure 2 in the main text.

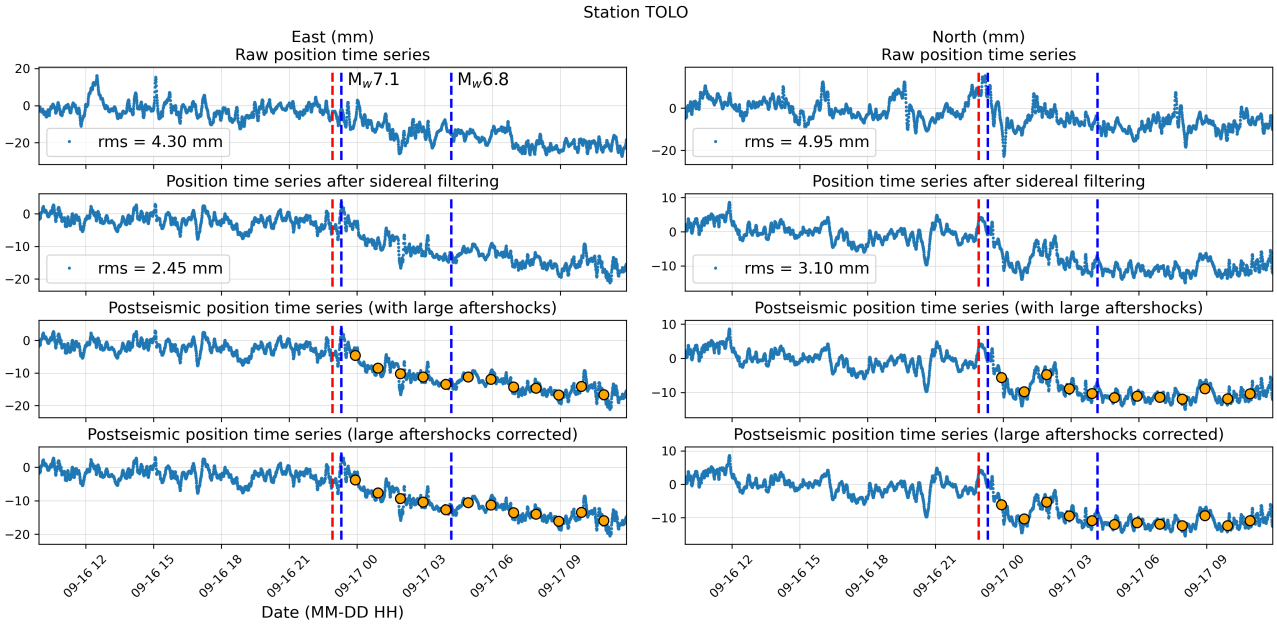

Figure S2.5. Same as Figure 2 in the main text.

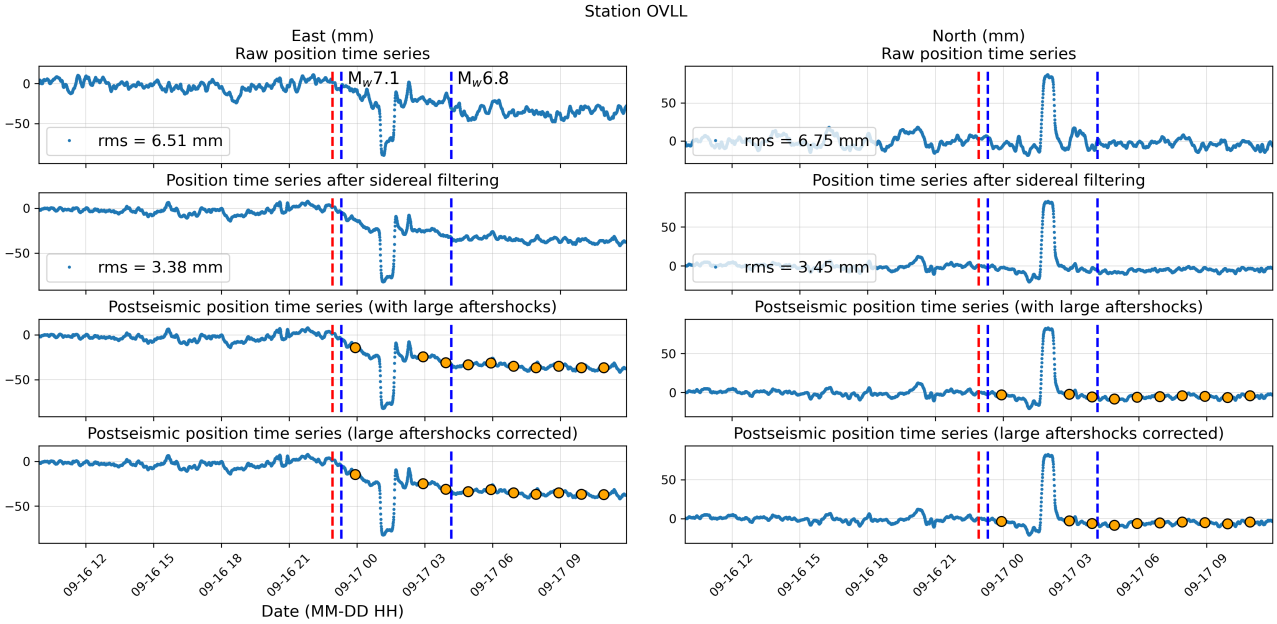

Figure S2.6. Same as Figure 2 in the main text.

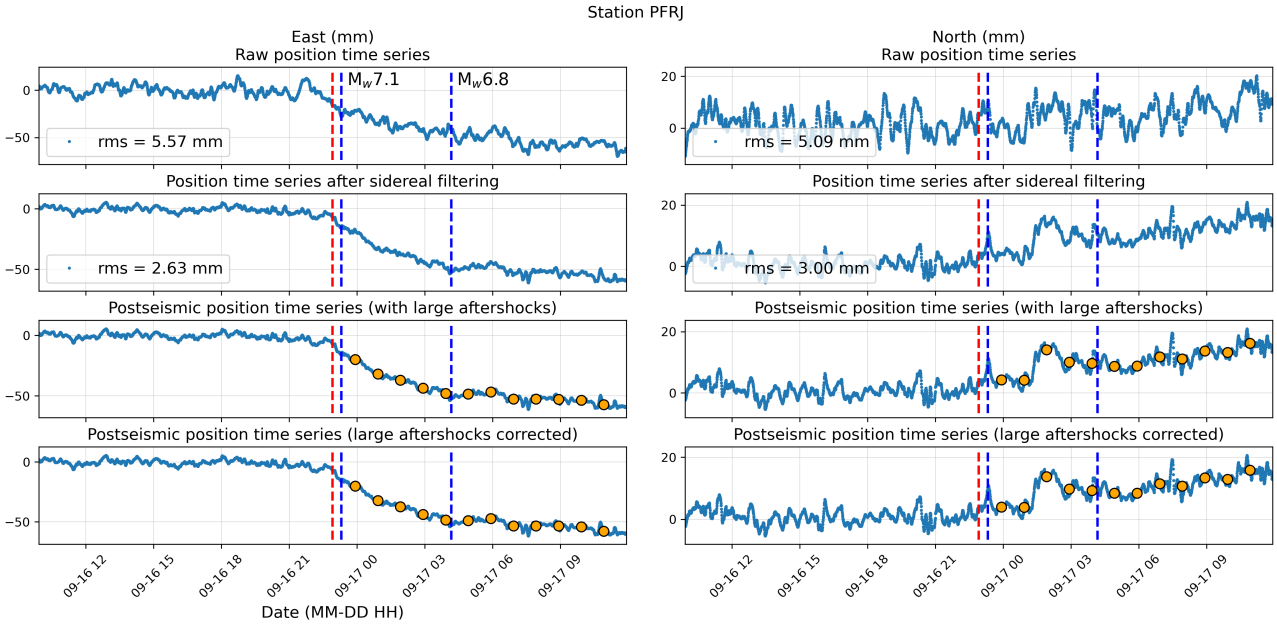

Figure S2.7. Same as Figure 2 in the main text.

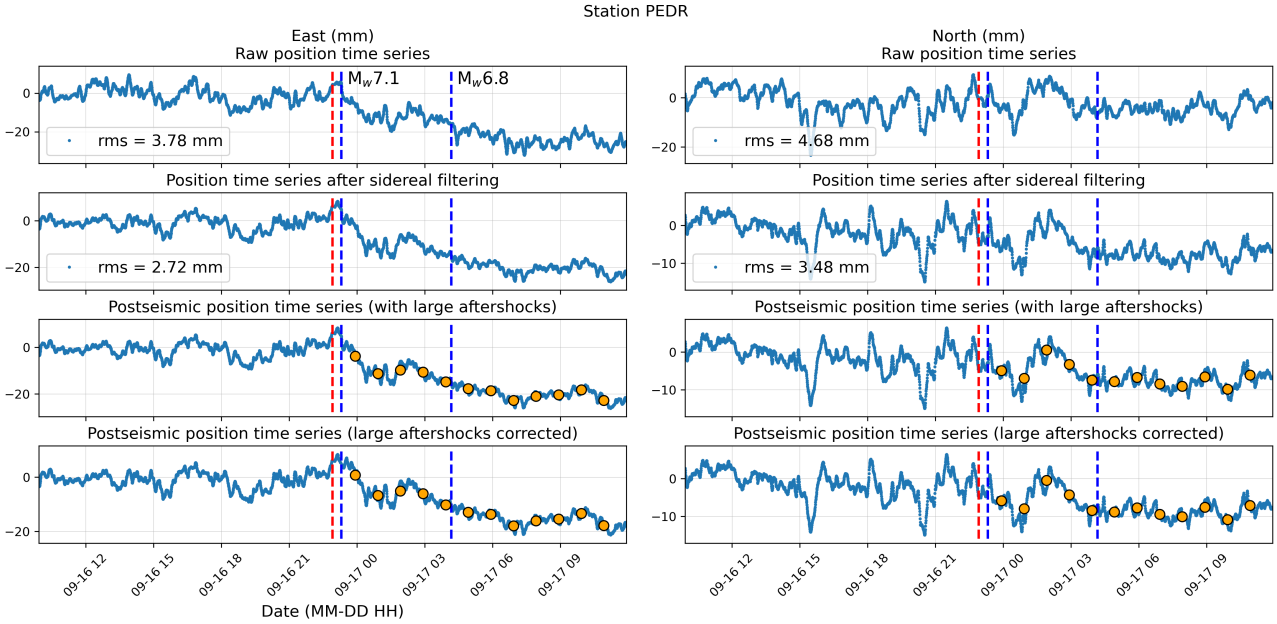

Figure S2.8. Same as Figure 2 in the main text.

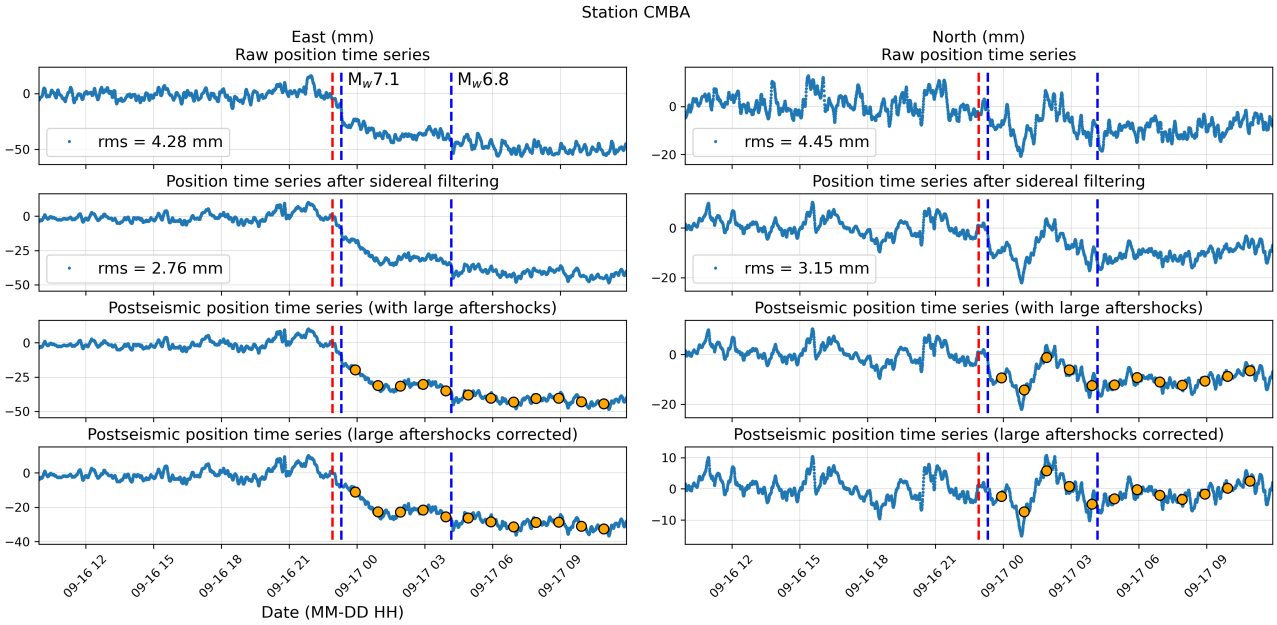

Figure S2.9. Same as Figure 2 in the main text.

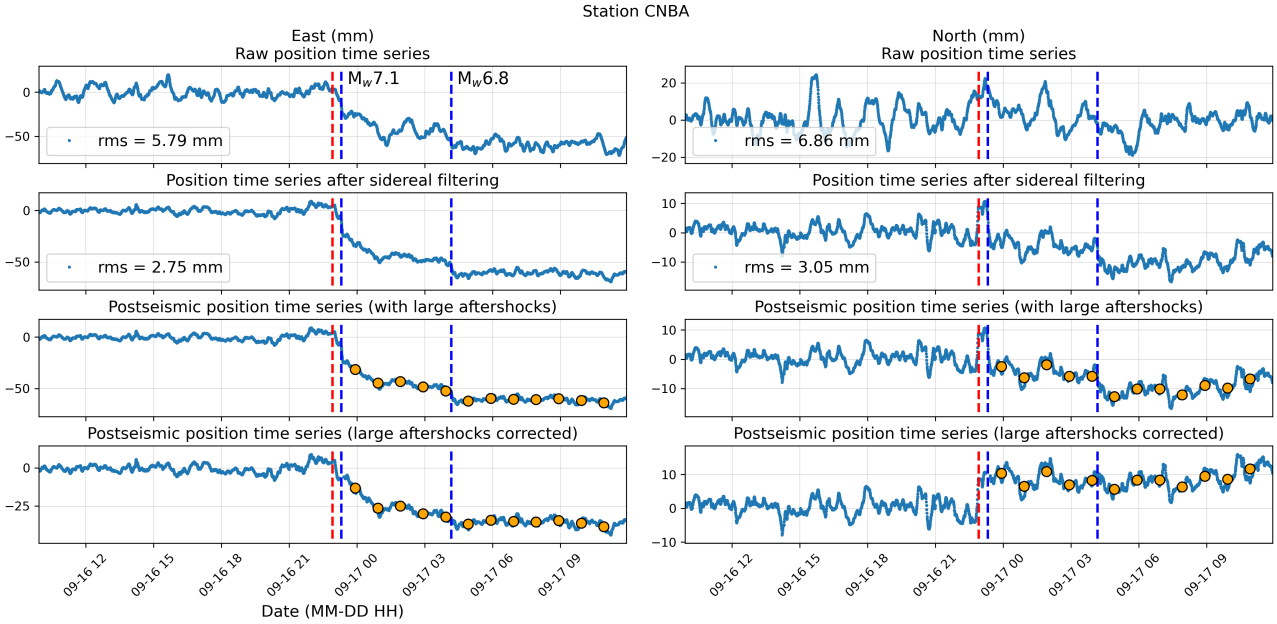

Figure S2.10. Same as Figure 2 in the main text.

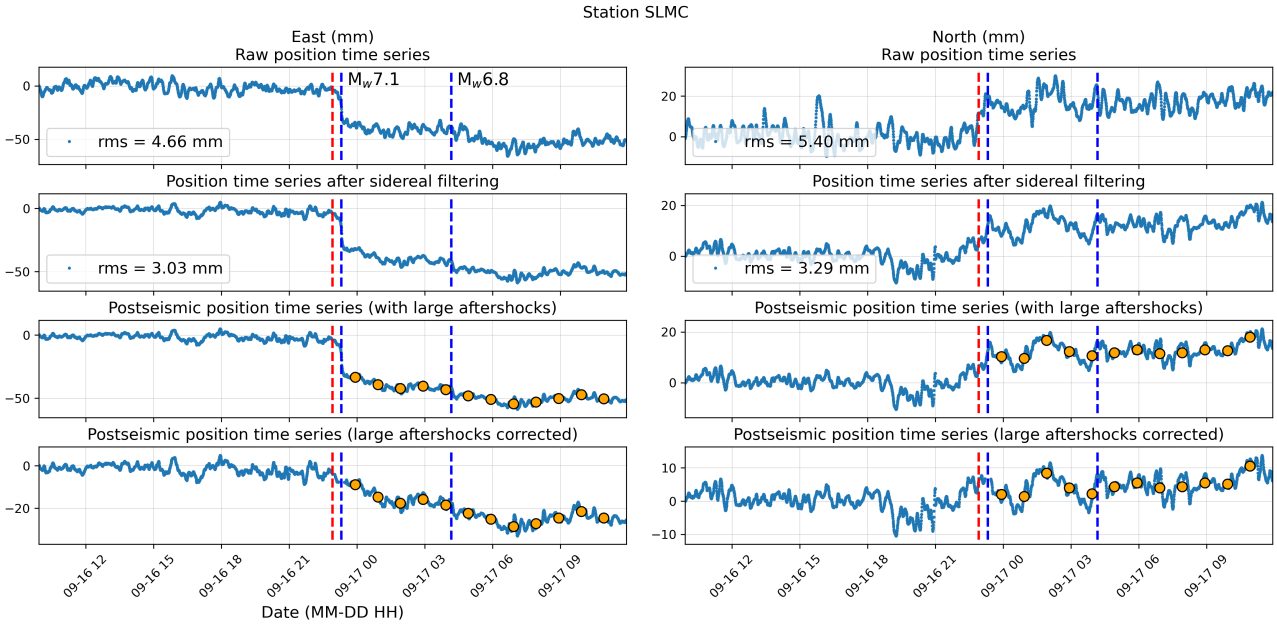

Figure S2.11. Same as Figure 2 in the main text.

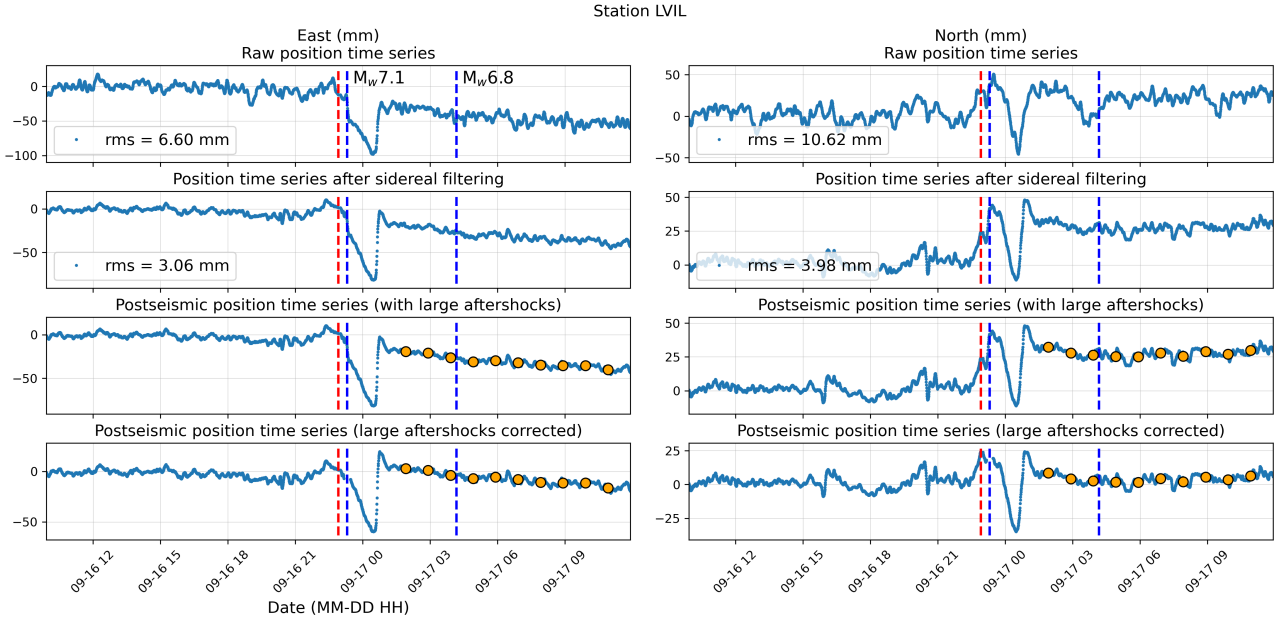

Figure S2.12. Same as Figure 2 in the main text.

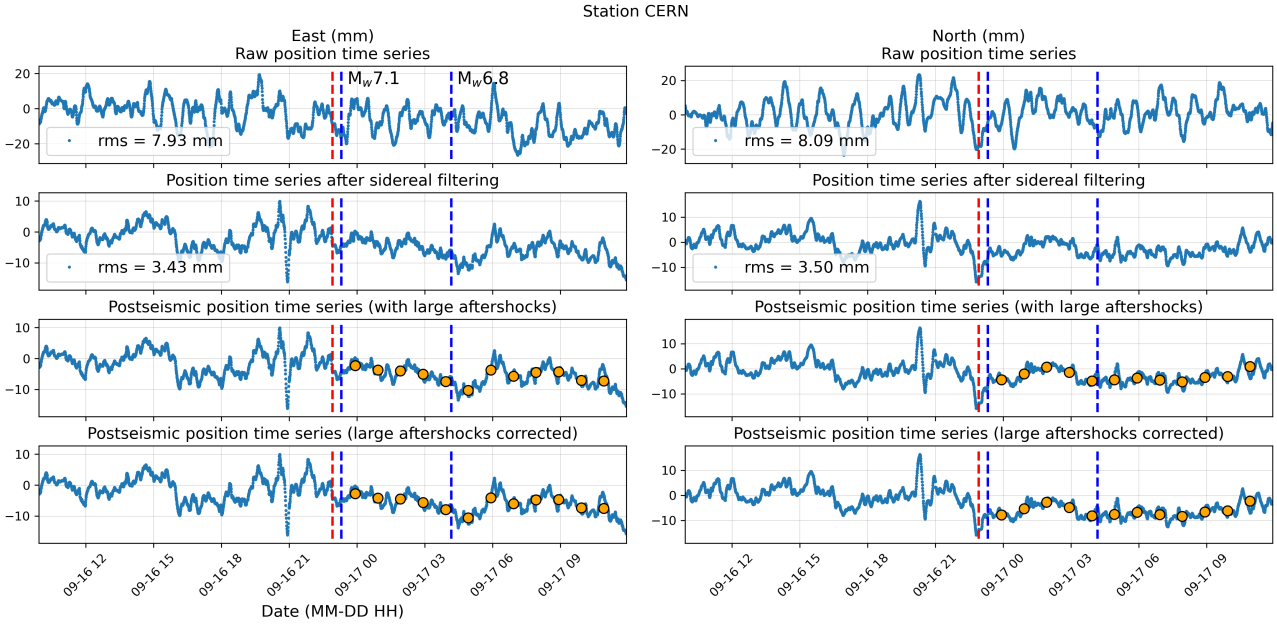

Figure S2.13. Same as Figure 2 in the main text.

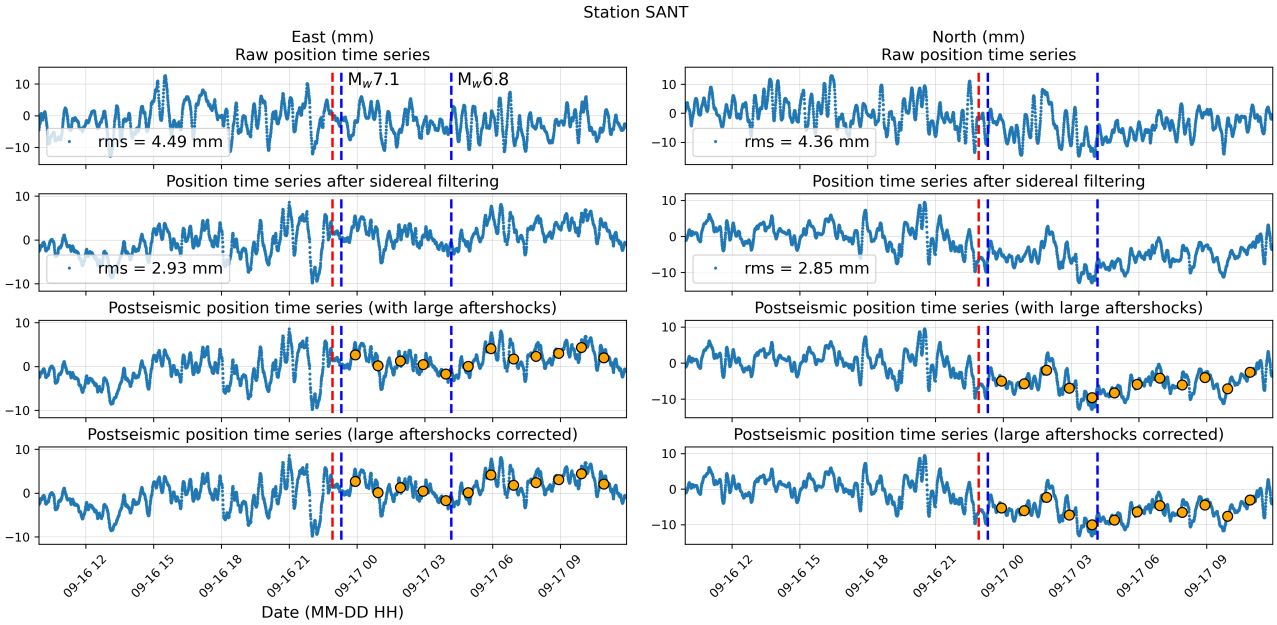

Figure S2.14. Same as Figure 2 in the main text.

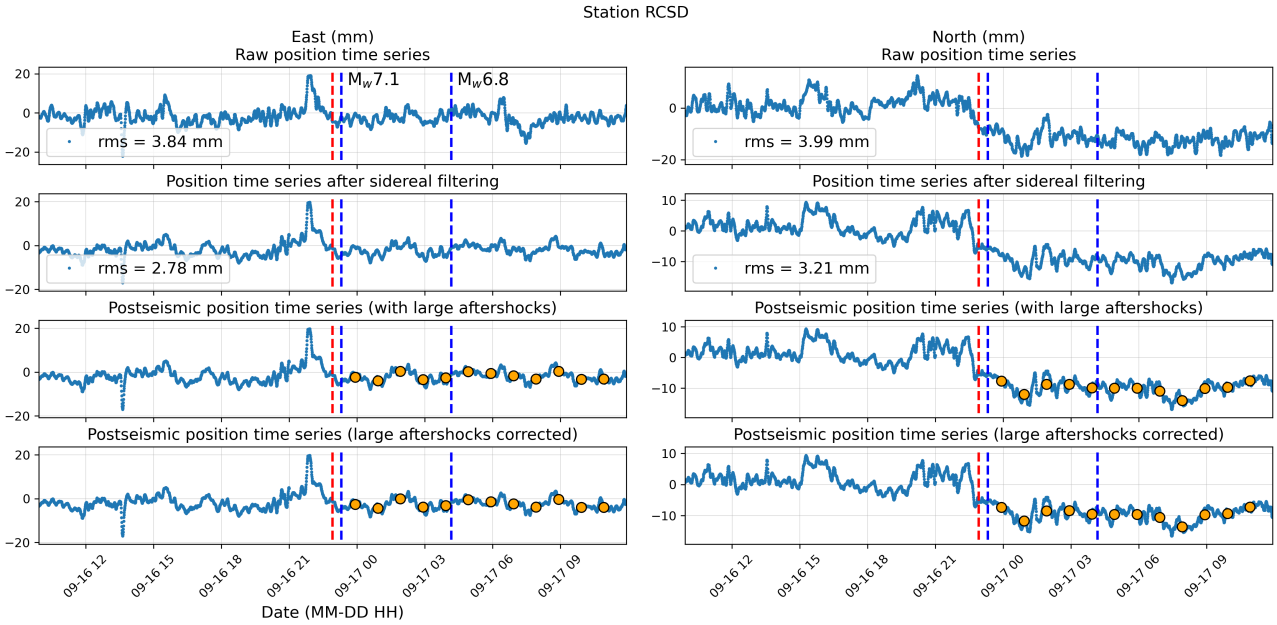

Figure S2.15. Same as Figure 2 in the main text.

S3 Choice of the smoothing parameter

As mentioned in the main text, the cost function has the following form:

$$\varepsilon = \frac{1}{N} \frac{\sum_{i=1}^{N} \left((o_i - c_i)/e_i\right)^2}{\sum_{i=1}^{N} o_i^2} + \omega\Lambda \tag{1}$$

where N is the number of observations (2 horizontal components $\times$ number of receivers), e is the error associated to the observation, Λ is the Laplacian of the slip distribution and ω is the weight given to the Laplacian. In order to choose ω we tested different values ranging from 1.0×10^{-6} and up to 1.0×10^{6}. We use the L curve criterion to select the optimum value (Hansen, 1992). Based on the results shown in Figure S3.1 we choose 0.1 as the optimum value (red dot on Figure S3.1).

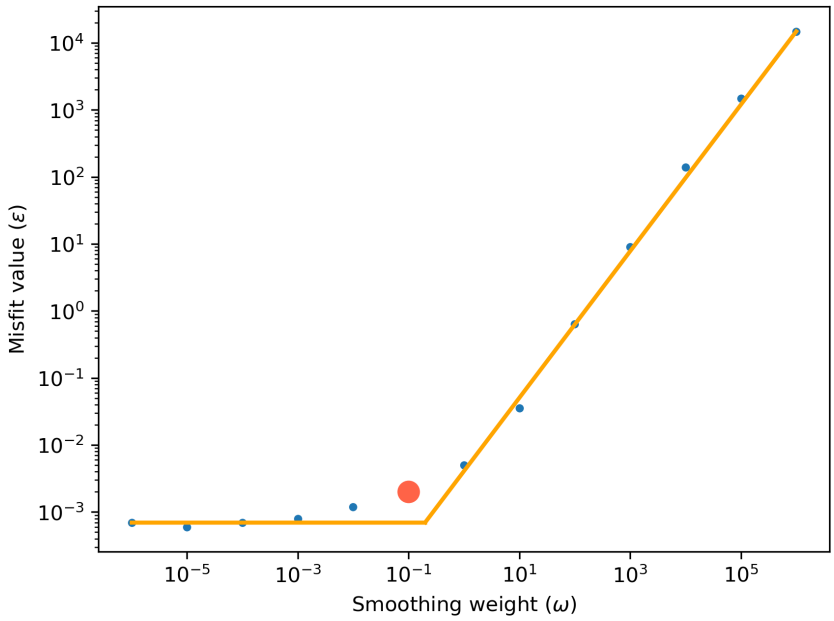

Figure S3.1. Evolution of the misfit as a function of the weight given to the Laplacian smoothing Λ (blue dots). The large red dot shows the selected value based on the L-curve criterion (Hansen, 1992). The orange line outline the trend.

S4 Summary of the results from the inversions.

In the following figures (Figure S4.1 to S4.15), we show a comparison between the observed position time series (blue) and the position time series calculated from the average post-seismic slip model (orange). Figure S4.16 shows a comparison between the observed and the calculated surface displacements in a map view at each time step. Finally, Figure S4.17 shows the rake angle for the average post-seismic slip model.

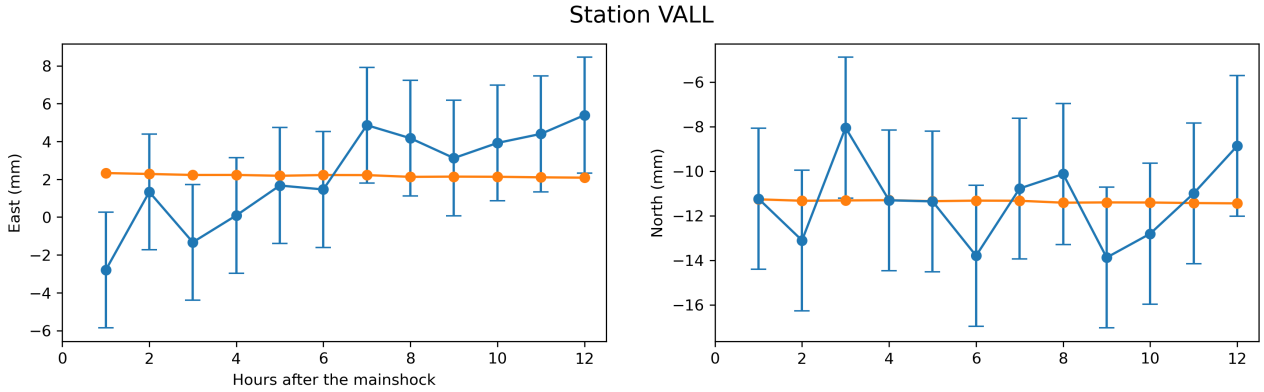

Figure S4.1. Blue dots show the observations along with their uncertainties, and the orange dots show the prediction from the average post-seismic slip model.

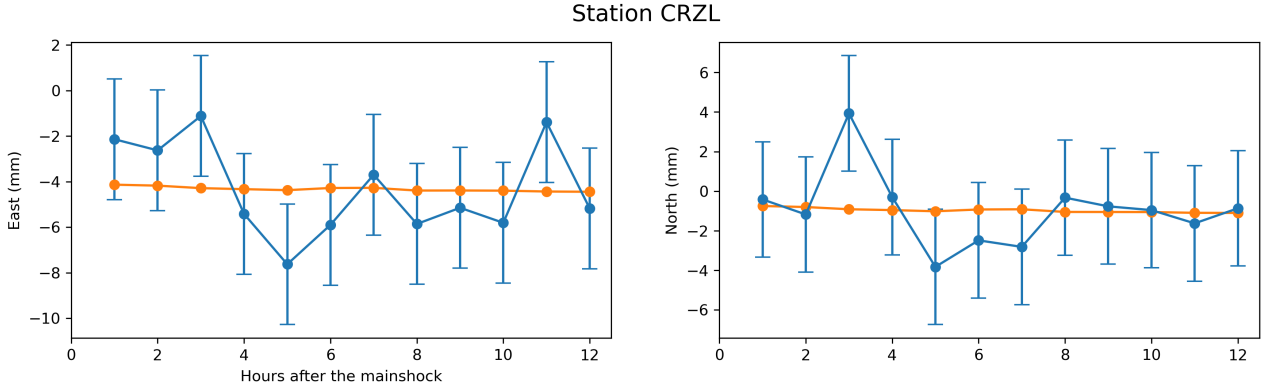

Figure S4.2. Blue dots show the observations along with their uncertainties, and the orange dots show the prediction from the average post-seismic slip model.

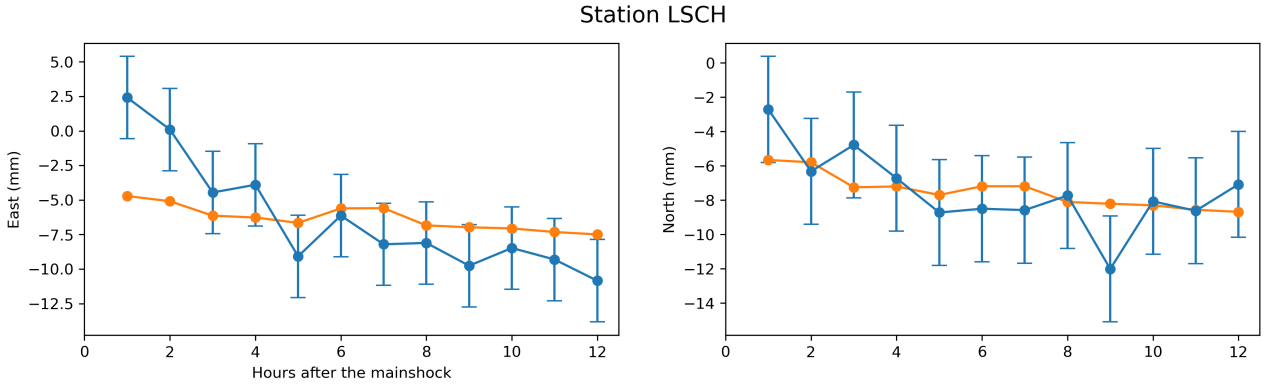

Figure S4.3. Blue dots show the observations along with their uncertainties, and the orange dots show the prediction from the average post-seismic slip model.

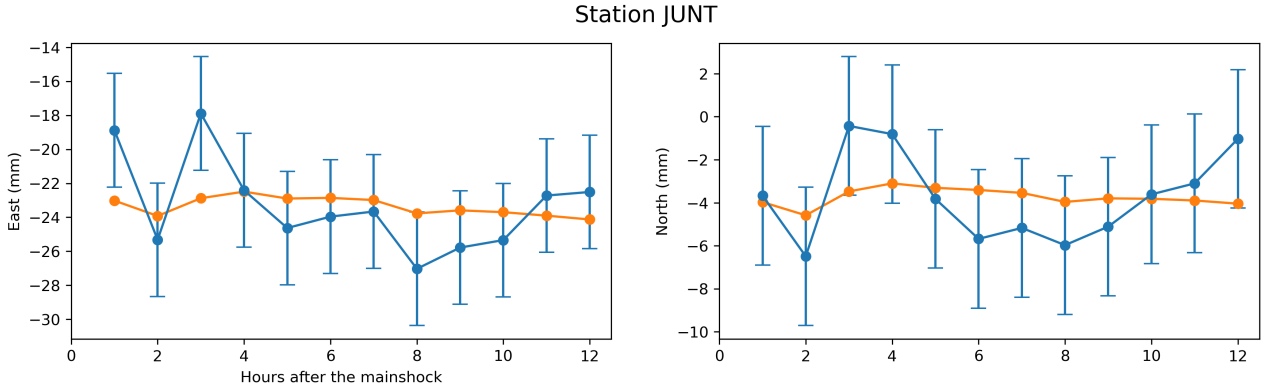

Figure S4.4. Blue dots show the observations along with their uncertainties, and the orange dots show the prediction from the average post-seismic slip model.

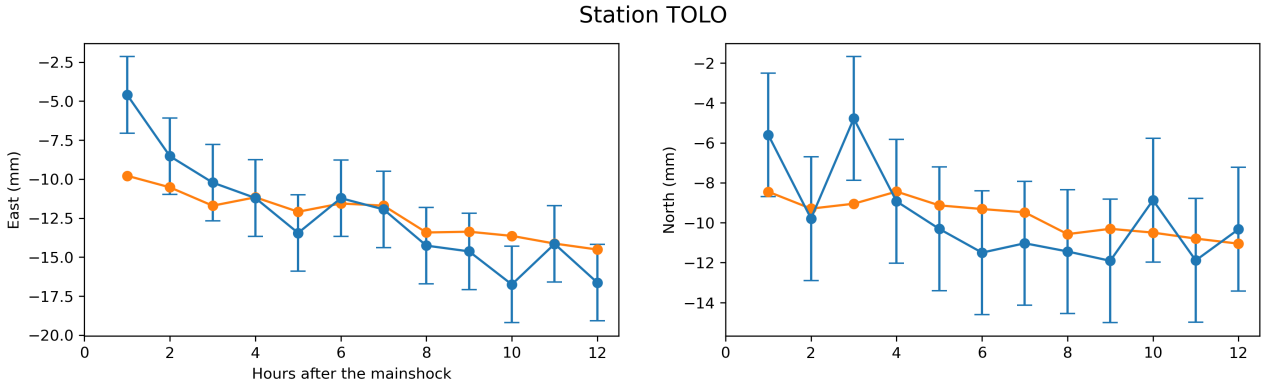

Figure S4.5. Blue dots show the observations along with their uncertainties, and the orange dots show the prediction from the average post-seismic slip model.

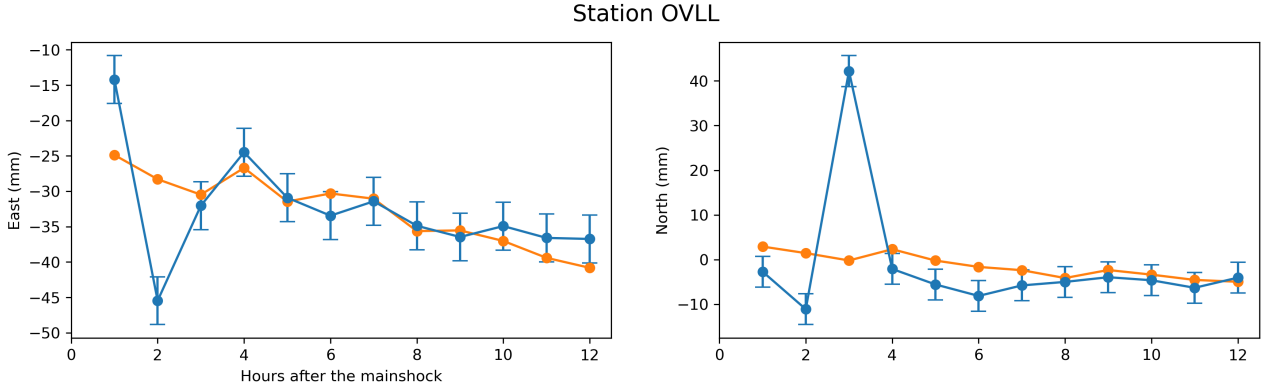

Figure S4.6. Blue dots show the observations along with their uncertainties, and the orange dots show the prediction from the average post-seismic slip model. As mentioned in the main text, hours 2 and 3 at this station are disregarded during the inversion because the high-rate position time series show strong spurious signal that are not of tectonic origin, which consequently affect the averaging.

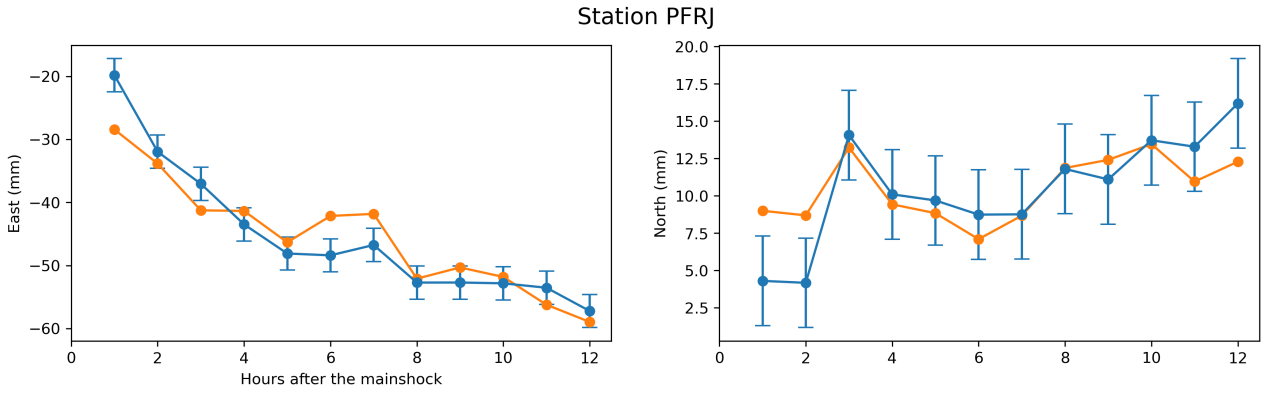

Figure S4.7. Blue dots show the observations along with their uncertainties, and the orange dots show the prediction from the average post-seismic slip model.

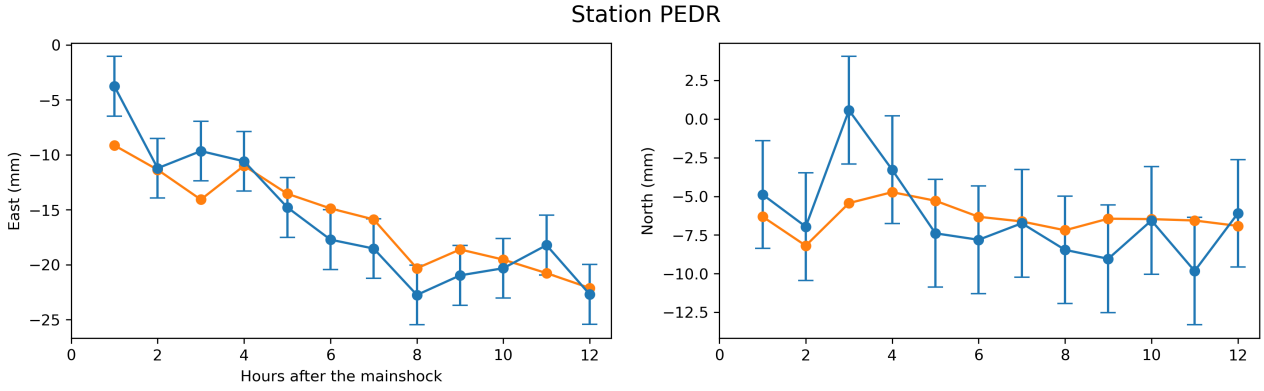

Figure S4.8. Blue dots show the observations along with their uncertainties, and the orange dots show the prediction from the average post-seismic slip model.Blue dots show the observations along with their uncertainties, and the orange dots show the prediction from the average post-seismic slip model.

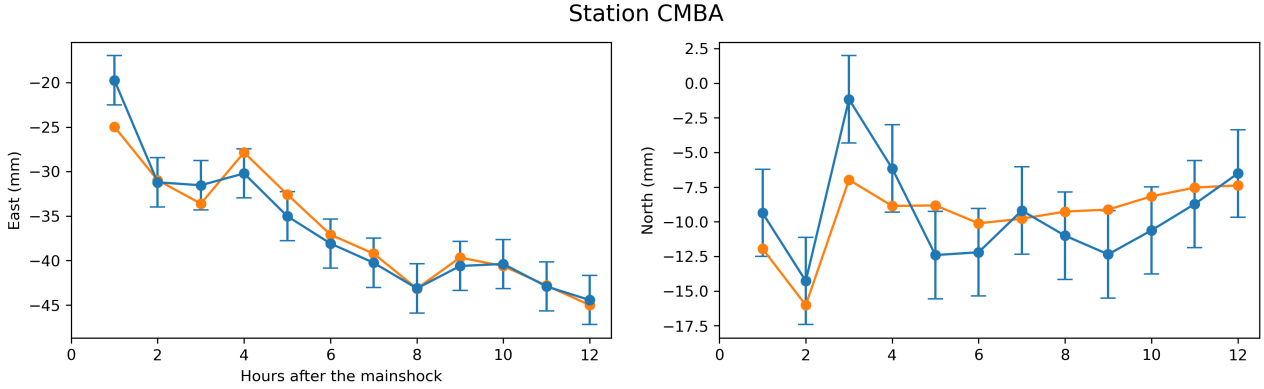

Figure S4.9. Blue dots show the observations along with their uncertainties, and the orange dots show the prediction from the average post-seismic slip model.

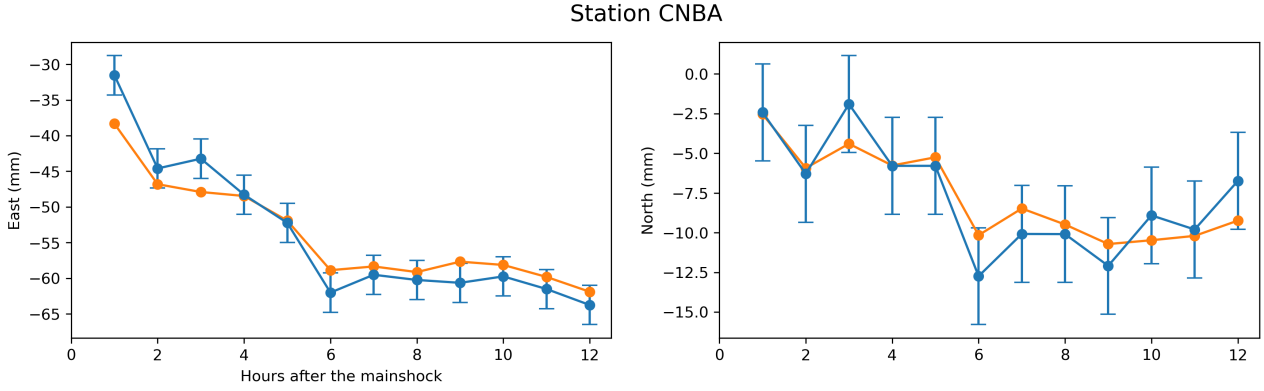

Figure S4.10. Blue dots show the observations along with their uncertainties, and the orange dots show the prediction from the average post-seismic slip model.

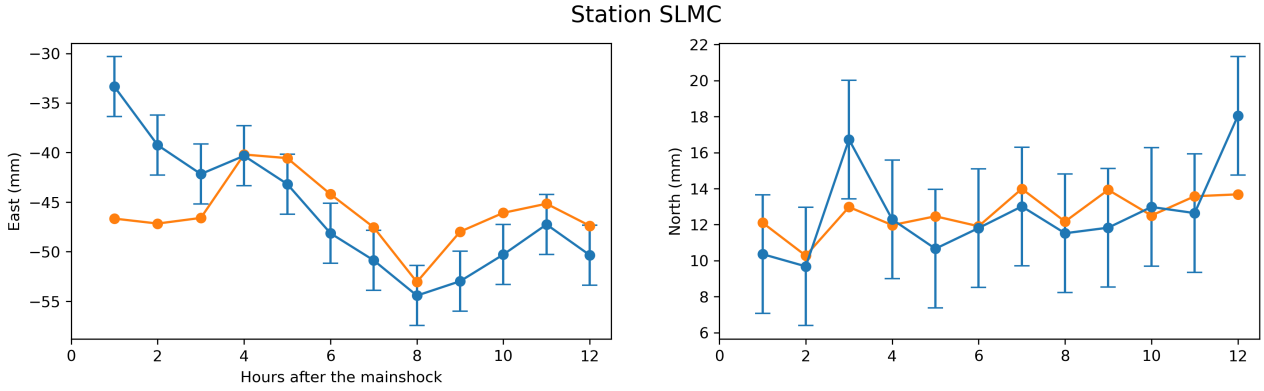

Figure S4.11. Blue dots show the observations along with their uncertainties, and the orange dots show the prediction from the average post-seismic slip model.

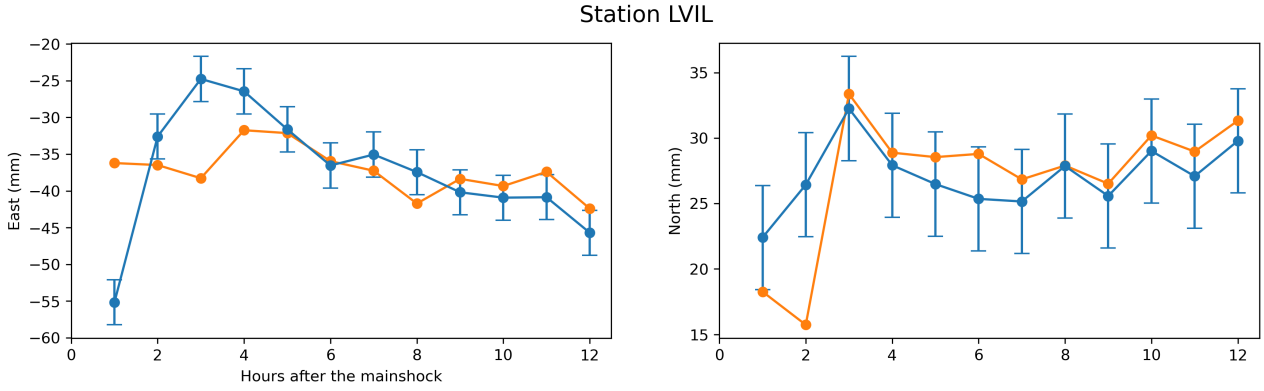

Figure S4.12. Blue dots show the observations along with their uncertainties, and the orange dots show the prediction from the average post-seismic slip model. As mentioned in the main text, the first 2 hours at this station are disregarded during the inversion because the high-rate position time series show strong spurious signal that are not of tectonic origin, which consequently affect the averaging.

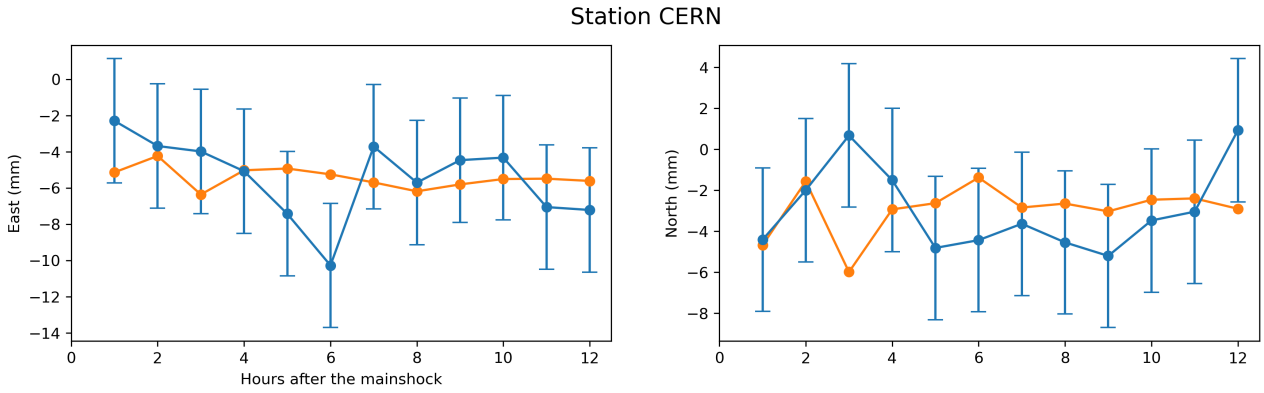

Figure S4.13. Blue dots show the observations along with their uncertainties, and the orange dots show the prediction from the average post-seismic slip model.

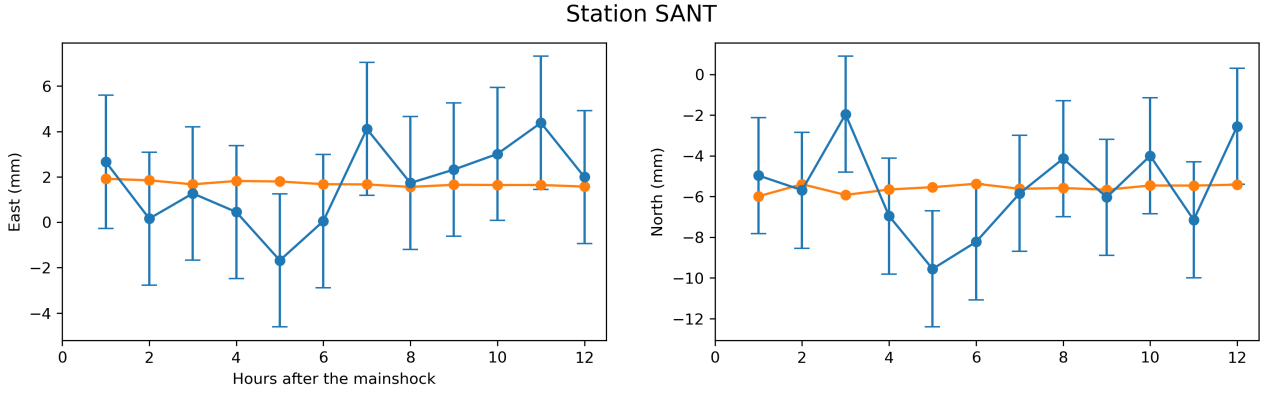

Figure S4.14. Blue dots show the observations along with their uncertainties, and the orange dots show the prediction from the average post-seismic slip model.

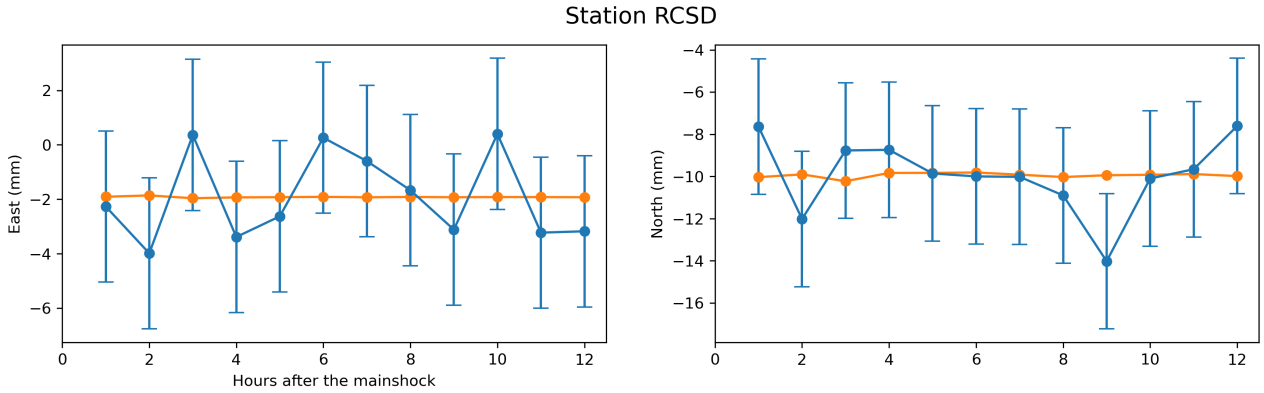

Figure S4.15. Blue dots show the observations along with their uncertainties, and the orange dots show the prediction from the average post-seismic slip model.

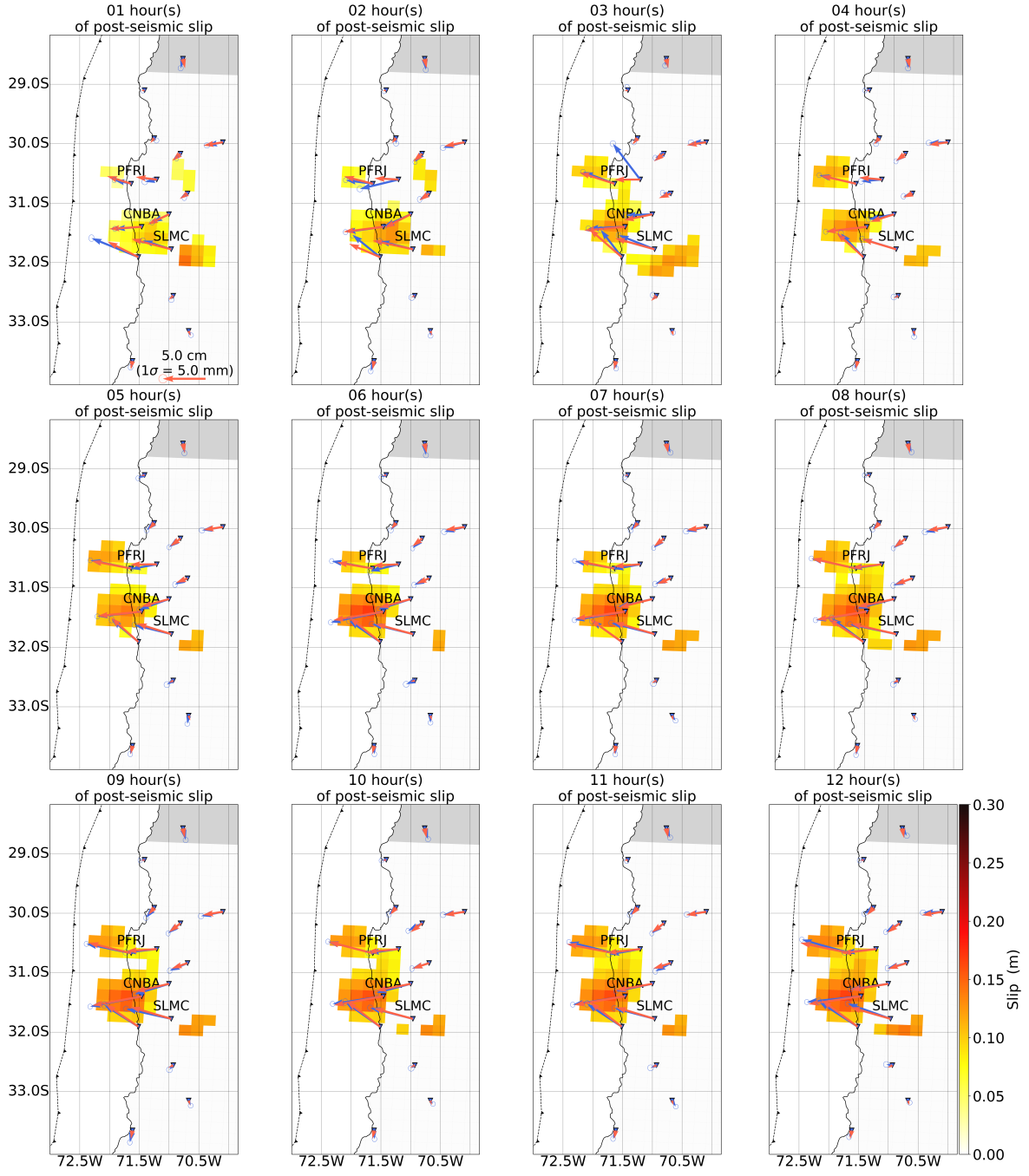

Figure S4.16. Map showing the observed horizontal displacements (blue arrows) and the predicted horizontal displacements (red arrows) for the average post-seismic slip model.

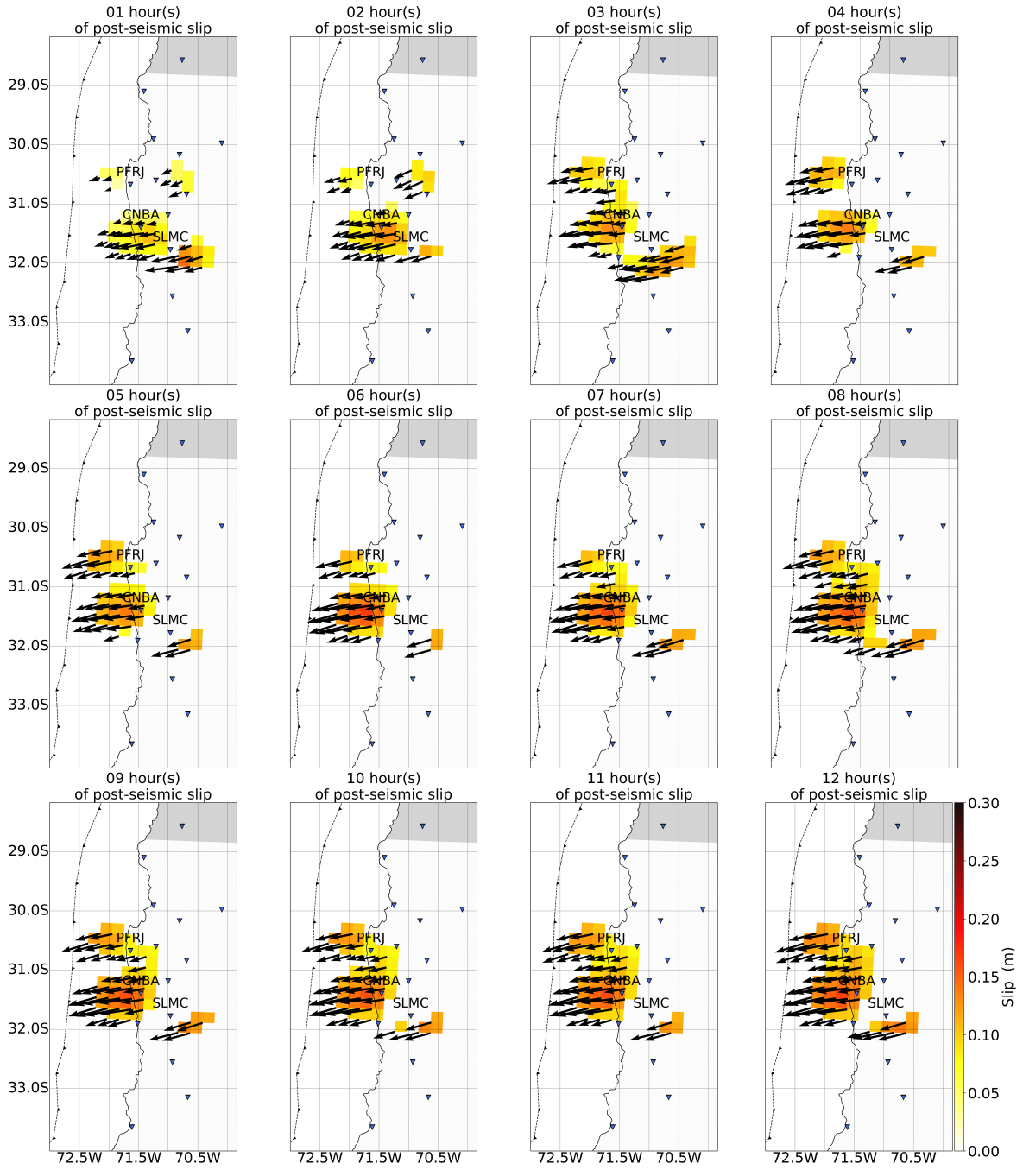

Figure S4.17. Map showing the obtained rake angle for the average post-seismic slip model. During the inversion the rake angle is allowed to vary by $\pm 15^{\circ}$ about the rake angle of the mainshock given by the GCMT catalog (i.e., 109°). The length of the arrows reflect the slip amplitude.

S5 Sensitivity analysis

In order to check the reliability of the afterslip models that we have obtained, we perform various sensitivity tests. First, we start by doing a resolution analysis. We compute the resolution matrix following Tarantola and Valette (1982):

$$R = C_m G^t \left(G C_m G.T + C_d\right)^{-1} G \tag{2}$$

where G are the Green's functions, C_d the data covariance matrix and C_m the model covariance matrix. The model covariance matrix is calculated using the ensemble of models that we have obtained from our inversion procedure after weighting each model by the inverse of the misfit. We first look at the diagonal elements of the resolution matrix (Figure S5.1a). This indicates if slip of a given subfault is correctly mapped to that particular subfault (Radiguet et al., 2011). We find the resolution appears rather low everywhere. This, is expected as the number of model parameters is large compared to the number of observation, an issue that is accounted for by introducing smoothing during the inversion. But the low resolution does not mean that slip cannot be recovered. Instead, it rather means that slip might not be recovered at the correct location (Page et al., 2009). Therefore, we investigate the strength of subfault-correlation by looking at the off-diagonal structure of R. In particular, we look at it for a subfault located at the center of the northern patch (Figure S5.1b) as well as for a subfault located at the center of the southern patch (Figure S5.1c). For both location, we find that slip is smeared out over a certain area, but it is not smeared much beyond the delineated areas that we use for the discussion in the main text. But, we notice that for the southern patch (Figure S5.1c), it is possible that some slip gets misallocated in a region that is south of station SLMC, which will be discussed later. However, overall, we find that the slip that we image in the northern and southern patches are likely to be relatively well located.

Another way that we can assess the reliability of the afterslip model is by looking at the relative standard deviation (RSD) and that is the ratio between the standard deviation and the mean model (Figure S5.2). We find that in the northern and the southern patch, the RSD is rather low suggesting that slip in these regions is well constrained, except for the first couple of hours in the northern patch. We also find that the deep region of afterslip located south-east of Salamanca (station SLMC) always has a large RSD. Thus, this region remains on the map simply because its amplitude is just a little bit higher than the standard deviation. That might suggest that this patch is rather unreliable. Based on the previous observation we made from looking at the resolution matrix, it is possible that this patch represents slip from the southern patch that is mis-located here because of a smearing effect.

Still, we further investigate the reliability of this deep patch of slip by looking at the impact it makes on surface displacements. Figure S5.3 and Figure S5.4 show the surface displacements induced by this patch at the surface on the north and east components, respectively. We only display regions where the amplitude of the surface displacements is larger than the lowest noise level among all the stations (i.e., 2.45 mm).

On the north component, we find that CERN and SLMC are potentially affected by the deep patch of afterslip, which contributes at most to -5.4 mm and 3.6 mm at these stations, respectively. For SLMC, we find that the contribution of that deep patch is very small compared to the observed displacement (see Figure S4.11), suggesting a rather negligible impact on the misfit. This is not so much the case for CERN (see Figure S4.13). However, the amplitude of the observed displacements on the north component at this station barely exceeds the noise level.

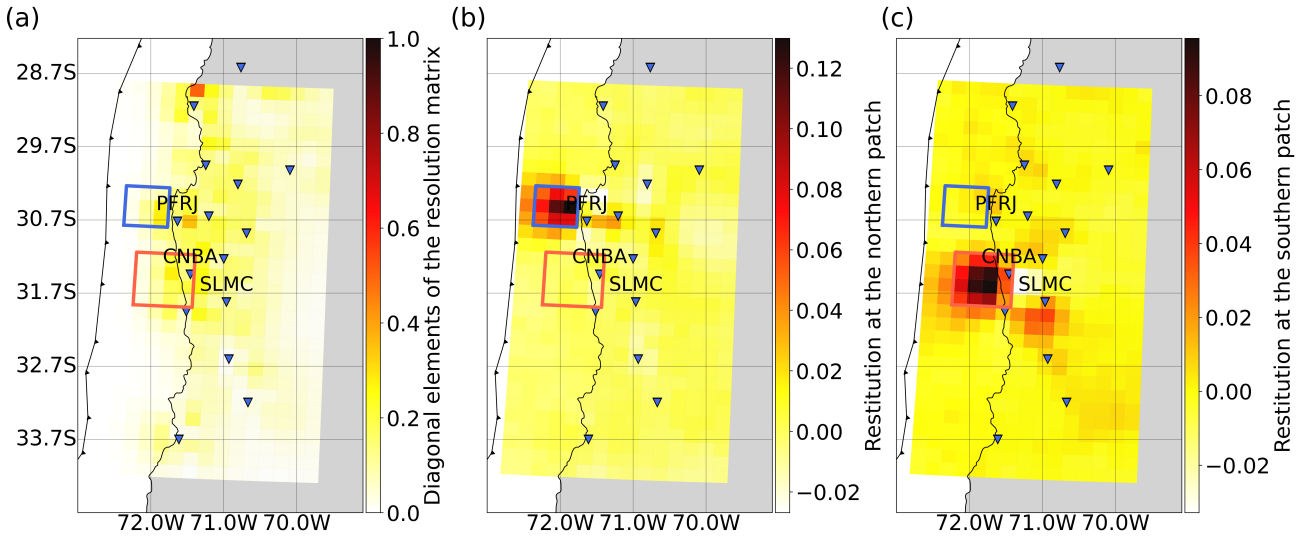

Figure S5.1. (a) Map of the diagonal elements of the resolution matrix. (b) Map showing the off-diagonal elements of the resolution matrix for a subfault that is located inside the northern patch discussed in the main text and highlighted by the blue square. (c) Map showing the off-diagonal elements of the resolution matrix for a subfault that is located inside the northern patch discussed in the main text and highlighted by the red square.

On the east component, we find that LVIL and SLMC are potentially affected. This time, it contributes at most to -6.0 mm and -4.2 mm at these stations, respectively. However, for both stations, we find that this contribution is quite small with respect to the observed surface displacements (see Figure S4.12 and Figure S4.11). Therefore, it is once again likely that this deep afterslip patch has a negligible impact on the misfit.

Two additional qualitative arguments can also be proposed as to why this patch is unreliable. First, Figure 3 in the main text shows that this patch does not exhibit a steady spatio-temporal evolution unlike all other regions of afterslip. That might reflect the fact that this patch helps to fit spurious signals in the time series rather than the manifestation of a transient phenomenon. Second, when we use the position time-series corrected from the 2 largest aftershocks (Figure 7 in the main text), we observe that the patch disappears almost completely. In our opinion, these arguments support even further the fact that this patch is likely to be unreliable rather than tectonically induced.

Therefore, based on these different arguments, we argue that this patch is not reliable, which is why we do not include it in the discussion in the main text.

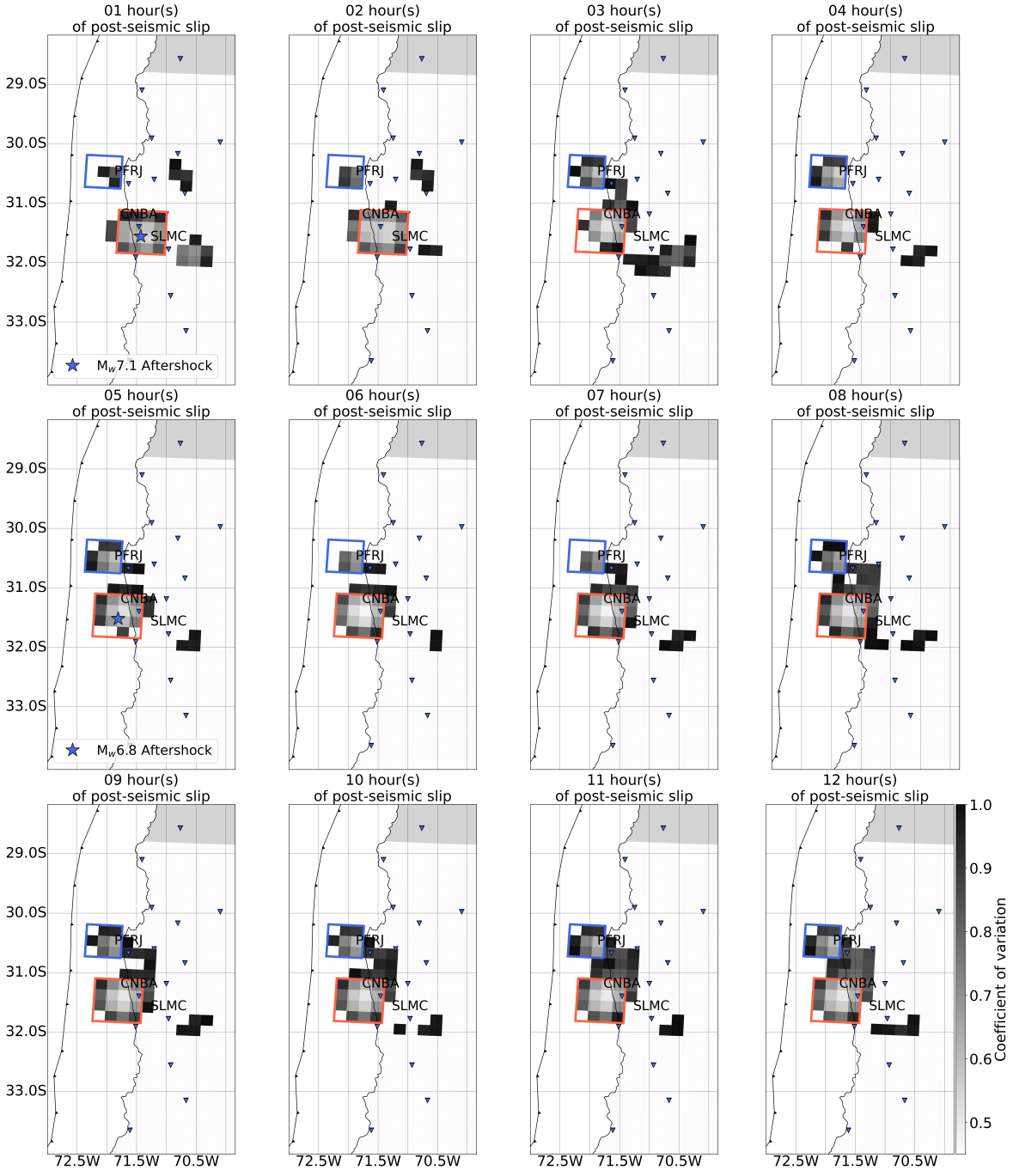

Figure S5.2. Maps of the coefficient of variation otherwise called the relative standard deviation (RSD) and that is the ratio between the standard deviation and the mean model.

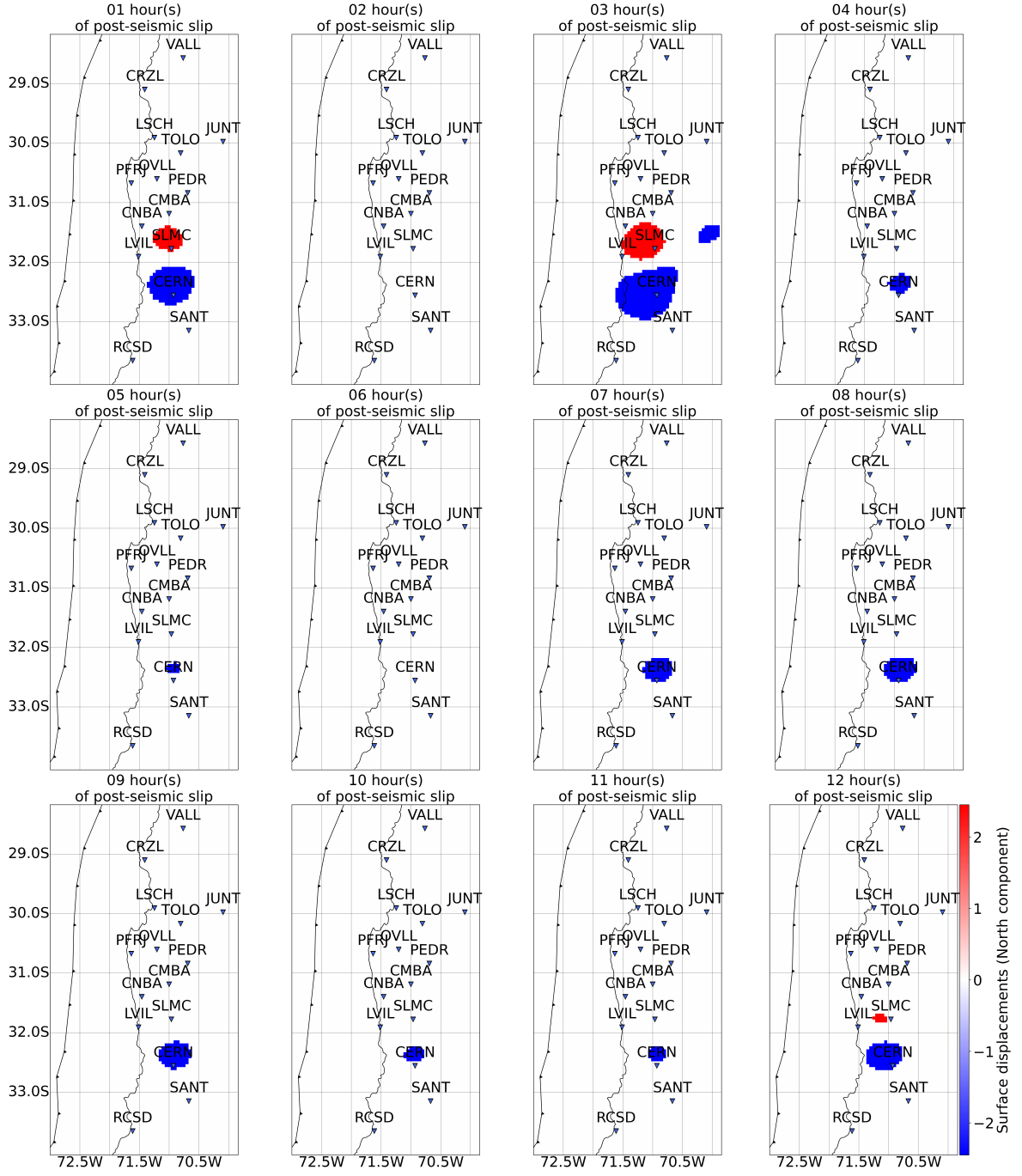

Figure S5.3. Surface displacements induced by the deep afterslip patch on the north component. The maps only show regions where the amplitude of the generated signal is larger than the lowest noise level among all stations (i.e., 2.45 mm)

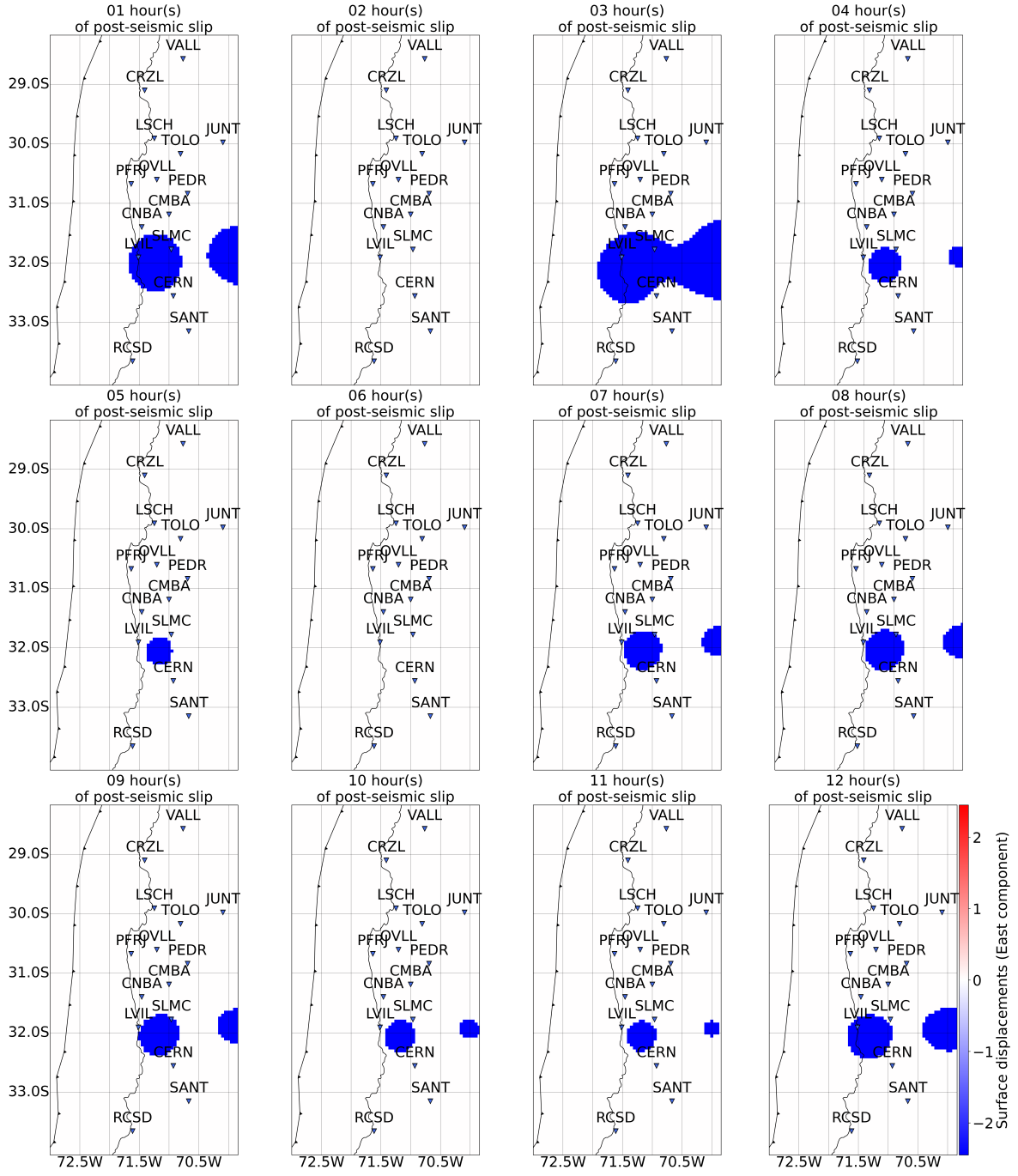

Figure S5.4. Surface displacements induced by the deep afterslip patch on the east component. The maps only show regions where the amplitude of the generated signal is larger than the lowest noise level among all stations (i.e., 2.45 mm)

S6 Comparison between the post-seismic slip model and various co-seismic slip models

Here, we compare the very-early post-seismic slip distribution after 12 hours with a non-exhaustive list of co-seismic rupture model from the literature (Figure S6.1). The model by Okuwaki et al. (2016) is the only one that is obtained using seismological data only (teleseismic waveforms). Thus, it is not at all contaminated by very-early afterslip. However, because only far-field data are used, it is likely that this model does not have the best resolution compared to the others. Melgar et al. (2016) uses the most complete dataset by including seismological data, tsunami data, high-rate GNSS data and InSAR data. Some contamination from very-early afterslip can be expected in the InSAR data since the tracks have been acquired 1 and 3 days after the mainshock. But, despite the fact InSAR data is used, most of the data are not contaminated by very-early post-seismic slip. Therefore, it is unlikely that the slip distribution contains a strong signature from the very-early post-seismic slip. This is why it has been chosen for the discussion in the main text. The model by Tillmann et al. (2015) is also obtained from a combination of seismological data and geodetic data (static offsets from GNSS data). Depending on the weighting adopted for each dataset, this model can be more or less affected by very-early post-seismic slip occurring during the first 12 hours. The remaining models presented are obtained using geodetic data only and are thus likely to be more or less contaminated by very-early afterslip. The model by (Shrivastava et al., 2016) is obtained using static co-seismic offsets measured from daily GNSS data. This is also the case for the model by (Ruiz et al., 2016). Then, the model by (Barnhart et al., 2016) is obtained by adding InSAR data. Finally, the co-seismic slip model obtained by Klein et al. (2017) comes from a combination of InSAR data, static co-seismic offsets from daily GNSS data and strict co-seismic offsets measured from high-rate GNSS data. Note that for almost all models, the 1-m slip contour is displayed on the figure (2-m for the model by Klein et al. (2017)).

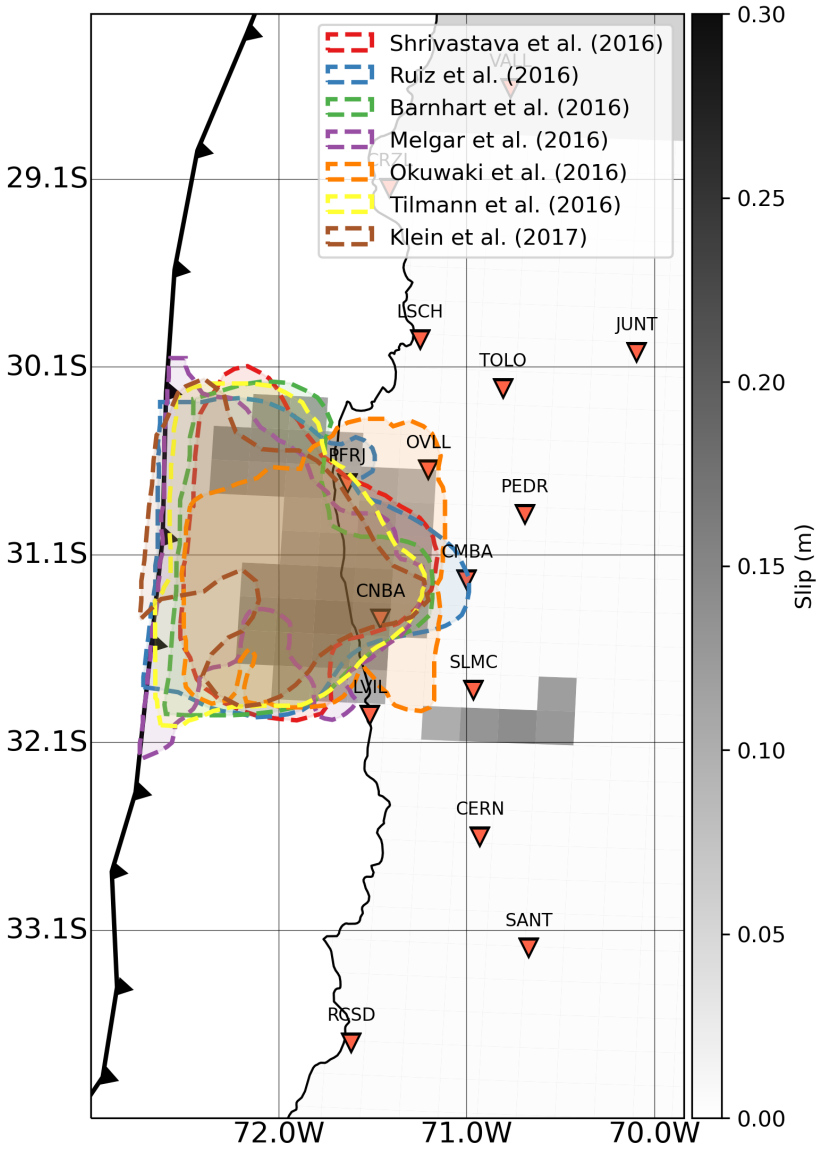
Shrivastava et al. (2016)
Ruiz et al. (2016)
Barnhart et al. (2016)
Melgar et al. (2016)
Okuwaki et al. (2016)
Tilmann et al. (2016)
Klein et al. (2017)
VALL
CRZL
LSCH
JUNT
TOLO
OVLL
PFRJ
PEDR
CMBA
CNBA
SLMC
LVIL
CERN
SANT
RGSD
29.1S
30.1S
31.1S
32.1S
33.1S
72.0W
71.0W
70.0W
0.30
0.25
0.20
0.15
0.10
0.05
0.00
Slip (m)

Figure S6.1.

S7 Comparison between very early post-seismic slip and very early aftershocks using Frank et al. (2017) catalog

In order to ensure that our conclusions are not strongly dependent on the chosen catalog, we also make a comparison between our post-seismic slip models and the catalog of aftershocks obtained from template-matching techniques by Frank et al. (2017). As shown by Figure S7.1, we observe an nearly identical pattern as what we observe using the catalog from Huang et al. (2017). Over the first 2 hours, most of the seismic activity occurs south of the rupture area, just as does the post-seismic slip. To the north, very little activity is seen during these first 2 hours but it then progressively intensifies just like the post-seismic slip. After the first 12 hours of the post-seismic phase, we see a pattern where post-seismic slip and aftershocks strongly overlap, both surrounding the co-seismic rupture area.

Finally, we also compare the afterslip and aftershock temporal evolution using the aftershocks catalog from Frank et al. (2017) to ensure our conclusions about their relationship are not dependent of the catalog. We find the same relationship between the cumulative afterslip and the cumulative number of aftershocks in the north patch (Figure S7.2).

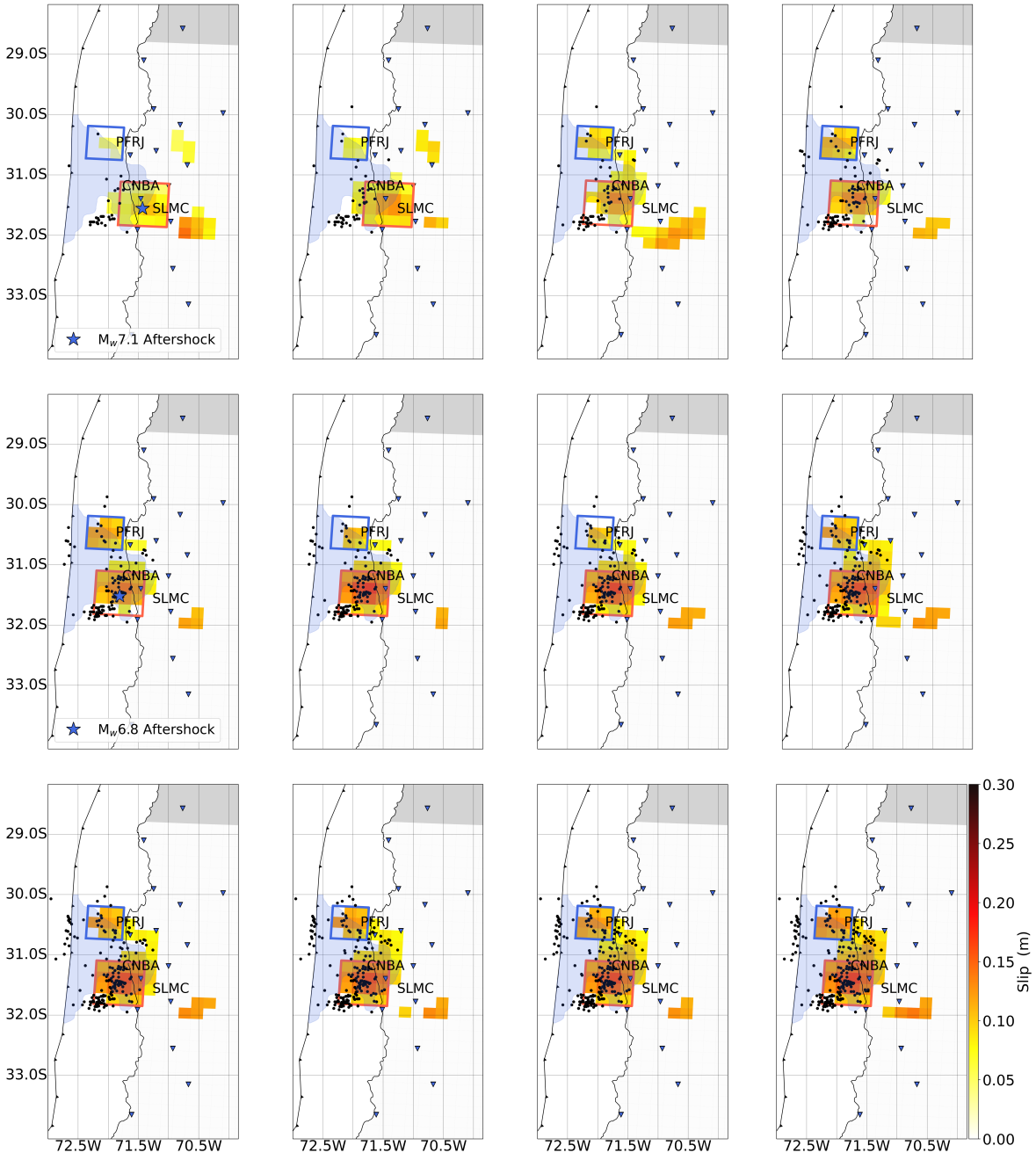

Figure S7.1. Same as Figure 5 in the main text, except that the aftershock catalog is from Frank et al. (2017).

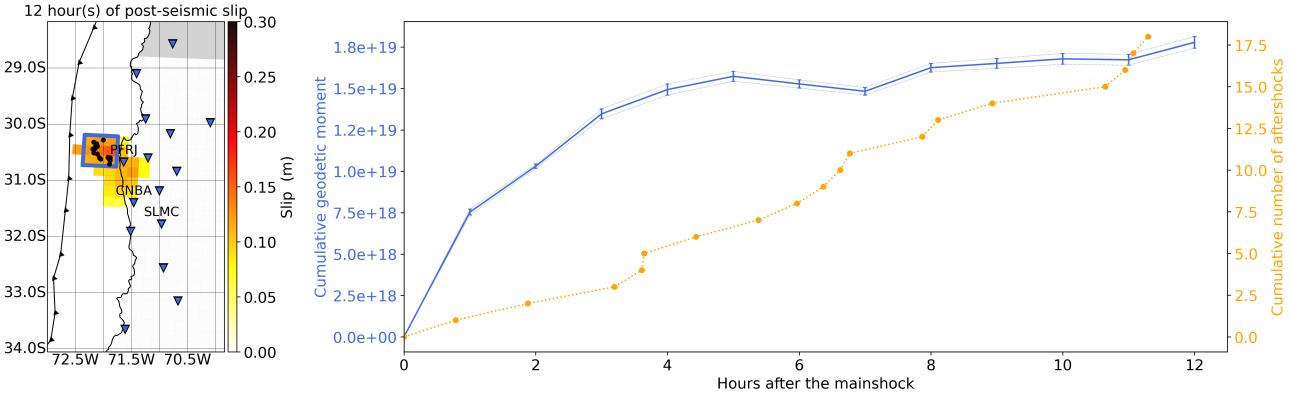

Figure S7.2. Same as Figure 8 in the main text, except that the aftershock catalog is from Frank et al. (2017).

References

Barnhart, W. D., Murray, J. R., Biggs, R. W., Gomez, F., Miles, C. P. J., Svarc, J., Riquelme, S., and Stressler, B. J.: Coseismic slip and early afterslip of the 2015 Illapel, Chile, earthquake: Implications for frictional heterogeneity and coastal uplift, J. Geophys. Res. Solid Earth, 121, 6172–6191, https://doi.org/10.1002/2016JB013124, 2016.

Frank, W. B., Poli, P., and Perfettini, H.: Mapping the rheology of central Chile subduction zone with aftershocks, Geophys. Res. Lett., 44, 5374—5382, https://doi.org/10.1002/2016GL072288, 2017.

Hansen, C.: Analysis of discrete ill-posed problems by means of the L-curve, SIAM Rev., 34, 561–580, https://doi.org/10.1137/1034115, 1992.

Huang, H., Xu, W., Meng, L., BB̈urgmann, R., and Baez, J. C.: Early aftershocks and afterslip surrounding the 2015 Mw 8.4 Illapel rupture, Earth Planet. Sci. Lett., 457, 282—291, https://doi.org/10.1016/j.epsl.2016.09.055, 2017.

Klein, E., Vigny, C., Fleitout, L., Grandin, R., Jolivet, R., Rivera, E., and Metois, M.: A comprehensive analysis of the Illapel 2015 M_w8.3 earthquake from GPS and InSAR data, Earth Planet. Sci. Lett., 469, 123–134, https://doi.org/10.1016/j.epsl.2017.04.010, 2017.

Melgar, D., Fan, W., Riquelme, S., Geng, J., Liang, C., Fuentes, M., Vargas, G., Allen, R. M., Shearer, P. M., and Fielding, E.: Slip segmentation and slow rupture to the trench during the 2015 M_w8.3 Illapel, Chile, earthquake, Geophys. Res. Lett., 43, 961–966, https://doi.org/10.1002/2015GL067369, 2016.

Okuwaki, R., Yagi, Y., Aranguiz, R., Gonzalez, R., and Gonzalez, G.: Rupture process during the 2015 Illapel, Chile earthquake: Zigzag-along-dip rupture episodes, Pure Appl. Geophys., 173, 1011–1020, https://doi.org/10.1007/s00024-016-1271-6, 2016.

Page, M., Custodio, S., Archuleta, R., and Carlson, J.: Constraining earthquake source inversions with GPS Data 1: resolution based removal of artifacts, J. Geophys. Res., 114, B01 314, https://doi.org/10.1029/2007JB00544, 2009.

Radiguet, M., Cotton, F., Vergnolle, M., Campillo, M., Valette, B., Kostoglodov, V., and Cotte, N.: Spatial and temporal evolution of a long term slow slip event: the 2006 Guerrero Slow Slip Event, Geophys. J. Int., 184, 816–828, https://doi.org/10.1111/j.1365-246X.2010.04866.x, 2011.

Ruiz, S., Klein, E., del Campo, F., Rivera, E., Poli, P., Metois, M., Vigny, C., Baez, J. C., Vargas, G., Leyton, F., Madariaga, R., and Fleitout, L.: The Seismic Sequence of the 16 September 2015 Mw 8.3 Illapel, Chile, Earthquake, Seism. Res. Lett., 87, https://doi.org/10.1785/0220150281, 2016.

Shrivastava, M. N., Gonzalez, G., Moreno, M., Chlieh, M., Salazar, P., Reddy, C. D., Baez, J. C., nez, G. Y., Gonzalez, J., and de la Llera, J. C.: Coseismic slip and afterslip of the 2015 M_w8.3 Illapel (Chile) earthquake determined from continous GPS data, Geophys. Res. Lett., 43, 10 710–10 719, https://doi.org/10.1002/2016GL070684, 2016.

Tarantola, A. and Valette, B.: Generalized non-linear inverse problems solved using the least square criterion, Rev. Geophys. Space Phys., 20, 219–232, https://doi.org/10.1029/RG020i002p00219, 1982.

Tillmann, F., Zhang, Y., Moreno, M., Saul, J., Eckelmann, F., Palo, M., Deng, Z., Babeyko, A., Chen, K., Baez, J. C., Schurr, B., Wang, R., and Dahm, T.: The 2015 Illapel earthquake, central Chile: A type case for a characteristic earthquake ?, Geophys. Res. Lett., 43, 574–583, https://doi.org/10.1002/2015GL066963, 2015.

Twardzik, C., Vergnolle, M., Sladen, A., and Avallone, A.: Unravelling the contribution of early postseismic deformation using sub-daily GNSS positioning, Sci. Rep., 9, https://doi.org/10.1038/s41598-019-39038-z, 2019.